OPEN ACCESS

ACTA METALLURGICA SLOVACA

2020, VOL. 26, NO. 1, 4-6

RESEARCH PAPER

EFFECT OF SALT BATH NITRIDING TIME ON THE PERFORMANCES OF 304 STAINLESS STEEL

*Xiliang LIU[1,3], Changjun Mao[1,3], Meihong WU[1,2], Wei CAI[1,2], Mingyang DAI[1], Jing HU[1,3]**

[1] School of Materials Science and Engineering, Jiangsu Key Laboratory of Materials Surface Science and Technology, Changzhou University, Changzhou 213164, China

[2]) School of Computer Engineering，Nanjing Institute of Technology，Nanjing 211167，China；

[3]) National Experimental Demonstration Center for Materials Science and Engineering, Changzhou University, Changzhou 213164

**Corresponding author: e-mail: jinghoo@126.com Tel.: +86 0519 86330095, School of Materials Science and Engineering, Jiangsu Key Laboratory of Materials Surface Science and Technology, Changzhou University, Changzhou 213164, China*

Received: 15.02.2020

Accepted: 24.02.2020

ABSTRACT

In this study, salt bath nitriding was carried out at 565℃ for various times for 304 stainless steel (304SS). The effect of salt bath nitriding time on the microstructure, micro-hardness and wear resistance was investigated systematically. The results showed a nitriding layer was formed during salt bath nitriding, and the thickness of effective hardening layer is duration dependant. The maximum microhardness value of 1200$HV_{0.01}$ was obtained at optimal duration of 150min, which was five times higher than that of the untreated sample. And the wear resistance could be significantly improved by salt bath nitriding, the lowest weight loss after wear resistance was obtained while nitriding for 150min, which was one tenth of that of untreated sample.

Keywords: 304 stainless steel; wear resistance; microhardness; salt bath nitriding

INTRODUCTION

Austenitic stainless steel has excellent corrosion resistance, but their surface hardness and wear resistance are poor [1-5]. In order to enlarge their real applications and meet the needs in various service environments, surface modification is essential to overcome these shortcomings.

Among the existed surface-modification techniques, nitriding treatment is one of the most widely used methods [6-10]. In real applications, there exist three kinds of normally used nitriding technologies, which are gas nitriding, plasma nitriding, and salt bath nitriding. And salt bath nitriding has highest efficiency and lowest production cost comparing the other two technologies [11-15].

Therefore, salt bath nitriding is conducted in this research, and the aim of the present study is to get rid of the empirical treating factors used by different users, and determine the optimum nitriding time of salt bath nitriding for 304 stainless steel by investigating the effect of nitriding time on the microstructure, microhardness and wear resistance, and thus the research will have important guiding significance to the industrial production in the salt bath nitriding for 304 stainless steel.

MATERIAL AND METHODS

The material used in this work is 304SS with the following chemical compositions (wt. %): C 0.06, Cr 18.64, Ni 9.31, Si 0.46, P 0.02, and Fe in balance. The substrate presented a microhardness of about 200$HV_{0.01}$.

Samples were cut in the size of 10×10×10 mm for microhardness test, and in the dimension of 32mm diameter and 5mm thickness disc for wear test. All of the flat surfaces of each sample were ground using various grades of SiC paper and polished to a mirror finish, and then ultrasonically cleaned in deionized water and alcohol for 5 minutes respectively before salt bath nitriding. The samples were pre-heated to 350℃ for 30min in air and then processed in tailor-made nitride salt bath with CNO^- concentration of 35% at 565℃ for various time (60min, 90min, 120min, 150min and 180min).

The cross-sectional microstructure of the samples was observed by optical metallography (XUG-05). The cross-sectional hardness was measured by Vickers microhardness tester at a load of 10 gf and the holding duration of 15s. Each hardness value was determined by averaging at least 5 measurements. The wear tests were carried out on a Wear Test Machine Type MMW-1A under ambient condition (20±2℃ and 50%RH). During the test, a 6 mm diameter GCr15 steel ball rotated at a speed of 200rpm on the surface of the samples for 60 min at a test load of 50N. The friction coefficient was continuously recorded during the test, and the weight of the samples before and after wear test was measured by a balance accurate to 0.1mg for calculating the weight loss.

RESULTS AND DISCUSSION

Metallographic observations

Fig. 1 shows the cross sectional microstructure of samples after salt bath nitriding for different nitriding time at 565℃. From the very surface to the core, a compound layer (bright layer) and diffusion layer are formed, and the compound layer thickness has no obvious difference with the duration increase from 60min to 180min. The diffusion layer is between bright-layer and matrix, which is hard to be clearly distinguished by optical microscopy, but can be determined by the effective hardening layer shown in the cross-sectional microhardness profile (Fig.2). Its main constitutions are solid solution or supersaturated solid solution of the N atoms (S-phase) in α-Fe, which could bring about an improvement of hardness comparing with the matrix [16-19].

DOI: 10.36547/ams.26.1.458

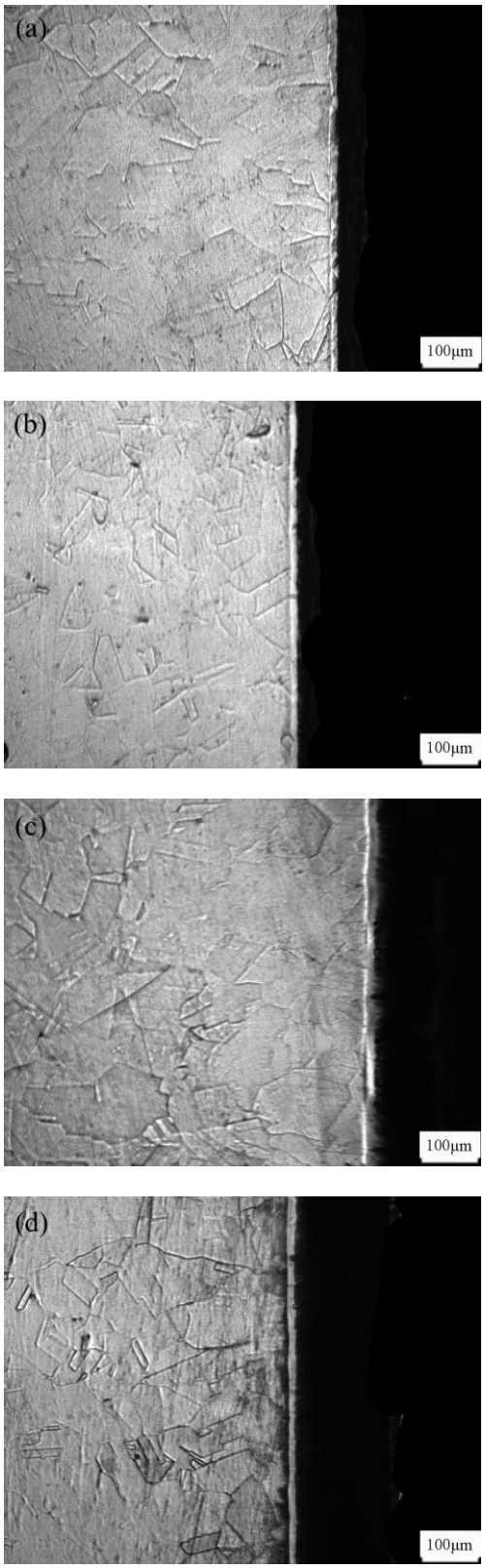

Fig. 1 The cross-sectional microstructures of specimens nitrided at 565℃for different time (a) 60min (b) 90min (c)120min (d)150min (e) 180min

Micro-hardness profile

Fig. 2 shows the microhardness profile for different nitriding time. The surface hardness reaches the maximum of 1200$HV_{0.01}$ when nitrided for 150min, which is 5 times higher than that of untreated sample of 200$HV_{0.01}$. With the increase of nitriding duration, the surface hardness and the effectively hardening layer increase gradually at first, and then turn to decrease slightly when the nitrided time exceeds 150min. The possible reason of this phenomenon is due to a loose structure formed on the top of the compound layer, and menwhile coarser grain size formed in the nitriding layer, resulting in the decrease of surface hardness once the nitrided time exceeding some duration [20-23].

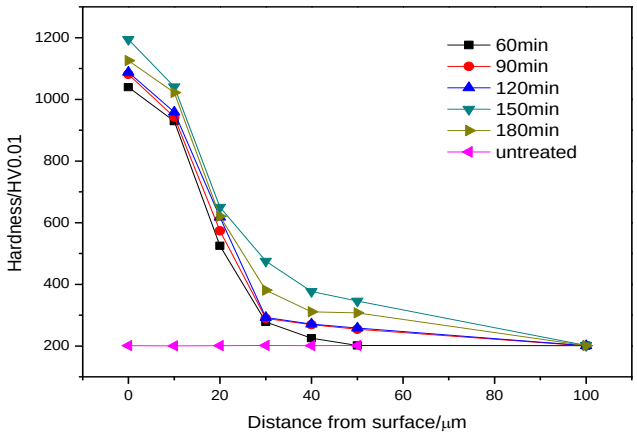

Fig. 2 The cross-sectional hardness profile of the specimens treated at 565℃ for different nitriding time

Wear resistance analysis

The variation of weight loss for untreated and nitrided samples is shown in Fig. 3. It can be clearly seen that the weight loss of the untreaded sample is much higher than those of nitrided samples, reaching around 0.09g. Whereas, the weight loss of samples after salt bath nitriding decreased dramatically, and a minimum of 0.0084g was obtained when nitrided for 150min, which is because a nitriding layer is formed on the surface after salt bath nitriding, resulting in excellent wear resistance. Meanwhile, it can be found that the weight loss has no obvious difference with the duration increase from 60min to 180min.

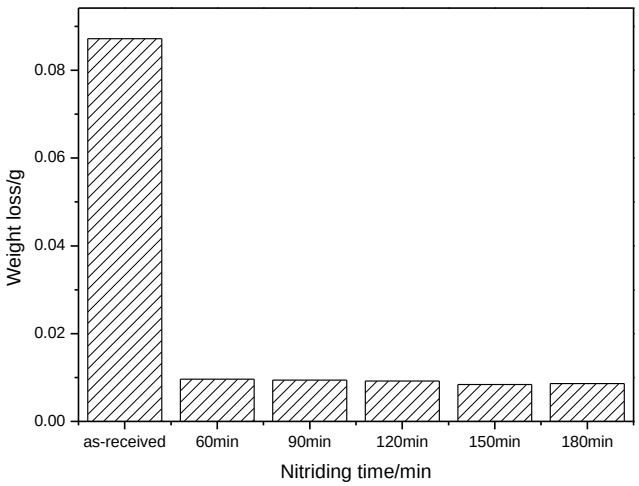

Fig.3 Weight loss of samples untreated and nitrided at 565 ℃ for different nitriding time

Fig.4 is the friction coefficient curve of the samples untreated and nitrided for different duration. It could be seen that the friction coefficient of nitrided 304SS was lower than that of the untreated samples. The average friction coefficient was 0.51 for the untreated sample, while decreased to some extent after nitriding, and the average friction coefficient is nitriding duration dependant, corresponding to 0.49, 0.46 and 0.42 for nitrding time of 60min, 90min and 150min, respectively. While it turned to be much rough for samples nitriding for 180min, possibly due to the looser surface formed at this long nitriding time.

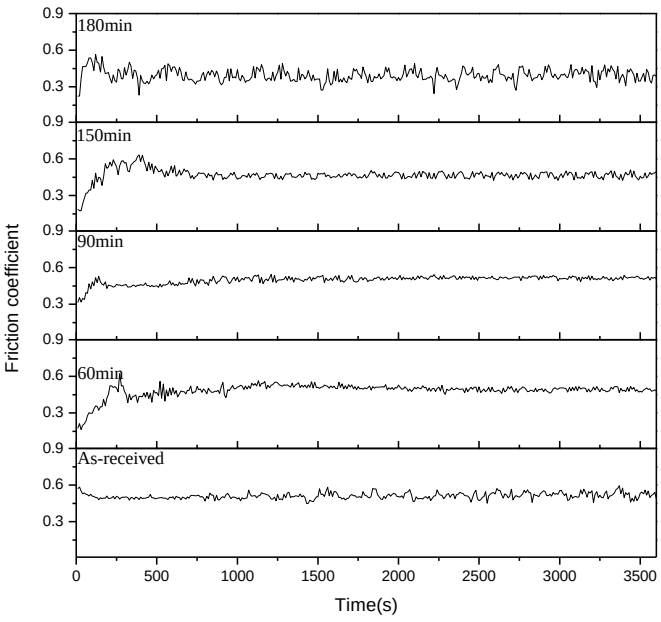

Fig.4 Friction coefficient of the samples samples untreated and nitrided for different time

CONCLUSION

(1) A nitriding layer was formed on the surface of 304SS after salt bath nitriding, and the thickness of the compound layer had no obvious difference with the duration increase from 60min to 180min.
(2) The optimal nitriding time was 150min for 304SS, with maximum surface hardness and best wear resistance.
(3) The surface hardness of 304SS was increased significantly after salt bath nitriding, reaching the maximum of $1200HV_{0.01}$, 6 times as high as $200HV_{0.01}$ of the untreated sample.
(4) The wear resistance of 304SS was improved dramatically after salt bath nitriding, the weight loss after wear test decreased to only 1/10 comparing with that of untreated sample.

Acknowledgments: Authors are grateful for the support of experimental works by projects of National Natural Science Foundation of China (21978025), Priority Academic Program Development of Jiangsu Higher Education Institutions (PAPD) and Top-notch Academic Program Projects of Jiangsu Higher Education Institutions.

REFERENCES

[1] W. Cai, F.N. Meng, X.Y. Gao, J. Hu: Applied Surface Science, Vol. 261, 2012, p. 411-414, doi: 10.1016/j.apsusc.2012.08.024.
[2] Y.Z. Shen, K.H. Oh, D.N. Lee: Scripta Materialia, Vol. 53, 2005, No. 12, p. 1345-1349, doi: 10.1016/j.scriptamat.2005.08.032.
[3] H.T. Fu, J. Zhang, J.F. Huang, Y. Lian, C. Zhang: Journal of Materials Engineering and Performance, Vol. 25, 2016, No. 1, p. 3-8, doi: 10.1007/s11665-015-1762-0.
[4] Z.S. Zhou, J. Hu: Surface Engineering, Vol. 25, 2015, No.1, p. 613-615, doi: 10.1179/1743294415Y.0000000076.
[5] X.Y. Ye, J.Q. Wu, Y.L. Zhu, J. Hu: Vacuum, Vol. 110, 2014, p. 74-77, doi: 10.1016/j.vacuum.2014.08.015.
[6] J.Q. Wu, H. Liu, X. M. Ye, Y.T. Chai, J. Hu: Journal of Alloys and Compounds, Vol. 632, 2015, No. 5, p. 397-401, doi: 10.1016/j.jallcom.2015.01.221.
[7] G. J. Li, Q. Peng, C. Li, et al.: Materials Characterization, Vol. 59, 2008, No. 9, p. 1359-1363, doi: 10.1016/j.matchar.2007.09.011.
[8] Z.S. Zhou, M.Y. Dai, Z.Y. Shen, J. Hu: Journal of Alloys and Compounds, Vol. 623, 2015, p. 261-265, doi: 10.1016/j.jallcom.2015.01.221.
[9] J.C. Li, X.M. Yang, S.K. Wang, K.X Wei, J. Hu: Materials Letters, Vol. 116, 2014, p. 199-202, doi: 10.1016/j.matlet.2013.11.033.
[10] M.Y. Dai, Y. Chen, Y. T. Chai, et al.: Surface Review and Letters, Vol. 23, 2016, doi: 10.1142/S0218625X16500499.
[11] Z.S. Zhou, M.Y. Dai, Z.Y. Shen, J. Hu: Vacuum, Vol. 109, 2014, p. 144-147, doi: 10.1016/j.vacuum.2014.07.016.
[12] Y. Li, L. Wang, D.D. Zhang, et al.: Journal of Alloys and Compounds, Vol. 497, 2010, No. 1-2, p. 0-289, doi: 10.1016/j.jallcom.2010.03.027.
[13] S.C. Gallo, H. Dong: Surface & Coatings Technology, Vol. 203, 2009, No. 24, p. 3669-3675, doi: 10.1016/j.surfcoat.2009.05.045.
[14] R.B. Huang, J. Wang, S. Zhong, M.X. Li, J. Xiong, H.G. Fan: Applied Surface Science, Vol. 271, 2013, p. 93–97, doi: 10.1016/j.apsusc.2013.01.111.
[15] J. Wang, Y.H. Li, J. Yan, D.Z. Zen, Q. Zhang, R.B. Huang, et al.: Surface & Coatings Technology, Vol. 206, 2012, No.15, p. 3399–3404, doi: 10.1016/j.surfcoat.2012.01.063.
[16] Y.S. Niu, R.H. Cui, Y.T. He, Z.M. Yu: Journal of Alloys and Compounds, Vol. 610, 2014, p. 294–300, doi: 10.1016/j.jallcom.2014.04.193.
[17] M.F. He, L. Liu, Y.T. Wu, C. Zhong, W.B. Hu, D. Pan: Journal of Alloys and Compounds, Vol. 551, 2013, p. 389–398, doi: 10.1016/j.jallcom.2012.11.005.
[18] G.J. Li, Q. Peng, C. Li, Y. Wang, J. Gao, S.Y. Chen, et al.: Materials Characterization, Vol. 59, 2008, No. 9, p. 1359–1363, doi: 10.1016/j.matchar.2007.11.002.
[19] R. Bidulský, J. Bidulská, M. Actis Grande: Metal Science and Heat Treatment, 58(11-12), 2017, 734-737. https://doi.org/10.1007/s11041-017-0087-z
[20] R. Bidulský, M. Actis Grande, M. Kabatova, J. Bidulská: Journal of Materials Science and Technology, 25(5), 2009, 607-610.
[21] R. Bidulsky, M. Actis Grande, E. Dudrova, M. Kabatova, J. Bidulska: Powder Metallurgy, 59(2), 2016, 121-127. https://doi.org/10.1179/1743290115Y.0000000022.
[22] J. Bidulska, R. Bidulsky, T. Kvackaj, M. Actis Grande: Materials, 12, 2019, 3724, https://doi.org/10.3390/ma12223724.
[23] R. Bidulský, M. Actis Grande, J. Bidulská, T. Kvačkaj: Materiali in Tehnologije, 43(6), 2009, 303-308.

OPEN ACCESS

ACTA METALLURGICA SLOVACA

2020, VOL. 26, NO. 1, 7-10

RESEARCH PAPER

MODELLING OF LASER POWDER BED FUSION PROCESS FOR DIFFERENT TYPE MATERIALS

Maria Rita Ridolfi[1], *Paolo Folgarait*[1,] *Andrea Di Schino*[2]

[1]*Seamthesis Srl, Piacenza, Italy*

[2)]*Università degli Studi di Perugia, Dipartimento di Ingegneria, Perugia, Italy*

**Corresponding author: andrea.dischino@unipg.it, Università degli Studi di Perugia, Dipartimento di Ingegneria, Via G. Duranti 93, 06125 Perugia, Italy*

Received: 09.03.2020
Accepted: 10.03.2020

ABSTRACT

The main problematic coming from the Laser Powder Bed Fusion (L-PBF) technique is the achievement of a fully dense part out of the interconnected tracks. The correct choice of process parameters is of fundamental importance to obtain a porosity free component. In this work, a model is described as able to simulate the printing process. The proposed model is a simplified numerical tool for designing processing windows suitable for metal alloys of any composition. The considered approach makes the model used as much practical as possible while keeping the physical description representative. The model is validated fitting experimental measures of track width, depth and cross-sectional area taken from three literature sources, referring to Ti6Al4V, Inconel 625 and Al7050. Effective liquid pool thermal conductivity, laser absorptivity and depth of application of laser energy are here considered as fitting parameters. Laser absorptivity and depth of application of laser energy result to rise almost linearly with increasing specific energy; the slopes of the three analyzed alloys result very close to each other. The obtained results give confidence about the possibility of using the model as a predicting tool after further calibration on a wider range of metal alloys.

Keywords: selective laser melting; additive manufacturing; modelling

INTRODUCTION

Laser Powder Bed Fusion (L-PBF) is one of the most adopted and successful powder bed fusion-based additive manufacturing technologies for many types of alloys including stainless steels and light alloys [1-6]. In L-PBF melting and solidification of a small powder, the volume is obtained using scanning on a powder layer by a laser. In the end, the partially overlapping tracks solidified or partially re-melted on any single layer are connected and the final component is manufactured. Main critical issues coming from this method concern the achievement of a fully dense part out of tracks interconnections. The target mechanical properties of a component (*e.g.* strength, ductility, creep and fatigue behaviours) strongly depend on the presence of porosities [7-18]. It is well known that process parameter correct determination a key issue to achieve porosity-free manufacture. It is also known that it strongly depends on powder composition morphology. The process parameter list includes the following topics: layer thickness, hatch, laser spot diameter and power. Finally, scanning speed needs to be considered. While layer thickness is affected by matters depending on the component target surface finishing degree resolution, the laser spot diameter is usually fixed on commercial 3d printers. The optimized process needs to take into account the determination of the best laser power and speed as well of the hatch distance. Therefore in order of selective laser melting process optimization, tools able to define the operating window in the *P-v* (laser beam power – velocity) space are needed. Such tools are required to take into account the dependence of such items on metals composition and powder morphology.

Several approaches have been developed for the above problem [19-22]. In the approach reported in [23], the process mapping simply gets to the process outcomes of an additive manufactured process, jus considering input power and speed. Usually, constant cross-sectional area curves are plotted to allow to determine the power and speed combinations resulting in a similar melt pool cross-sectional area.

Numerical modelling of the track melting has been approached by the use of commercial finite element software's [24-26].

In particular [27] reports about experiments carried out at the National Institute of Standards and Technology (NIST) on an Inconel 625 plate using an EOSINT M270 Laser Powder Bed machine. A test matrix of several powers and speed values combinations was originated, covering the full standard operating region of the considered 3D printer. Laser process simulations were carried out using a 3D finite element model. Results of the simulation were compared with the experimental cross-sectional areas. A not perfect fitting was obtained using a fixed value of effective laser absorptivity of 0.57, inducing to hypothesize better fitting for an absorptivity varying with laser power and speed.

In this paper, we propose a modelling tool able to generate processing maps of alloys suitable to the laser powder bed fusion technique. A simplified physical frame is modelled to reduce computing time. The model is then applied covering process parameters ranges typical of the specific additive manufacturing machine. The output is the limits of the conduction, transition and keyhole modes in the laser power-velocity plane, along with the full dense region.

Experimental data concerning different thermo-physical alloys properties are needed to validate the model. Three data sources have been selected throughout the literature at this first step of the model evolution [28-33].

The model

The continuous modification of the melt pool as the specific laser energy is due to the gas/melt surface evaporation onset and occurs when the temperature is high enough. The conduction mode ends up and a recoil momentum [10] is produced modifying the initially flat gas/melt interface and leading to an increasingly deeper cavity as the laser entering specific energy is enhanced. As the cavity deepens, higher energy values are absorbed into the cavity due to multiple ray reflections against the cavity interface [29]. Due to this mechanism, a shallow

cavity intercepts less energy than a deep keyhole cavity, resulting in a continuous increase of the effective laser absorbance of the interface achieving its minimum in the conduction mode; afterwards increasing in the transition mode, until reaching the maximum close to unity, for a fully developed keyhole. The absorbance minimum value is strictly correlated to the natural absorptivity of the metal alloy. As a consequence, the melt pool geometry transforms turning from wide and flat into narrow and deep.

The model is developed using the finite volume technique aimed to better take into account the gas cooling effect and its dependence on its vector properties and is described in detail in [34].

To achieve a simplified representation of the welding process, two main assumptions are performed:

1. avoiding evaporation and keyhole formation of explicit simulation. Heat transfer is modelled in terms of conduction through the melt pool for any operating condition input. This implies an accurate model validation and calibration for properly taking into account how much evaporation and formation of the cavity affect the melt pool geometry and overall heat transfer conditions.
2. modelling the powder layer as a continuum material, which thermo-physical properties come from a local powder particles arrangements, leading to the formation of sites where the powder is packed or rarefied (as the effect of the mixture with the gas).

RESULTS

The first applications, herein discussed, refer to single tracks generated over a single powder layer and have been used to calibrate the model using consistent experimental data [27-29].

The applied strategy to gain fitting results involves two different stages. In the first stage, the input laser specific energy is raised from the lowest level, the height h is set to an initial value and the laser absorptivity is given as first attempt the value competing to the simulated metal alloy, as deduced from available databases of metal surfaces reflectivity. Both h and α keep constant values for all operating conditions resulting in conduction mode.

The calibration when simulating the conduction mode is addressed at fitting measured depth and width data and at obtaining the boiling conditions in the weld pool at operating conditions experimentally marking the passage from conduction to evaporation. Experimental data employed in this work provide numerous track measures at different P-v values, scanning over the operating ranges of P and v with quite fine resolution, allowing for precisely detecting the transition from conduction to evaporation and keyhole formation. Laser absorptivity and effective thermal conductivity in the liquid pool are set as fitting parameters. Up to now, the calibration experience shows almost no need to vary the laser absorptivity derived from literature and web repositories referring to each metal alloy.

In the second stage, height h and α are varied with varying laser parameters until fitting measured values of depth and width. In particular, absorptivity increases with increasing the input laser specific energy until reaching a plateau at a value close to unity. Laser efficiency η has been kept constant and equal to 0.85.

The comparison between measured and calculated cross-sectional data are reported in Figure 1, in terms of width and depth data concerning the analysis performed on Ti6Al4V [28] (Figure 1a), Inconel 625 [29] (Figure 1b) and of the cross-sectional area for Al7050 [27] (Figure 1c).

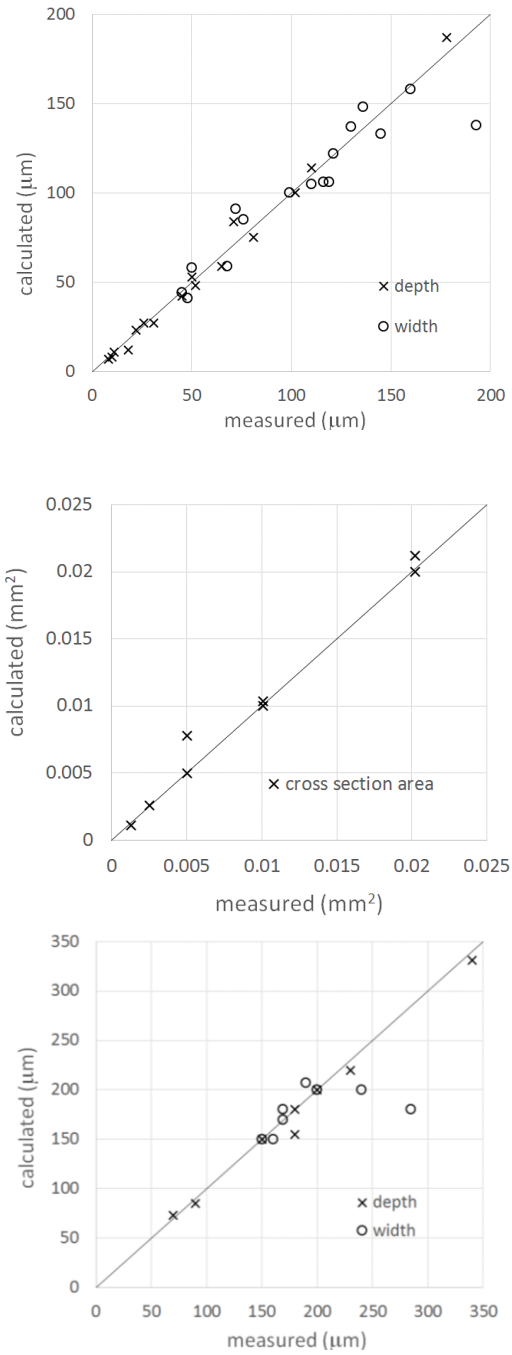

Fig. 1 Comparison between measured and calculated data of Ti6Al4V track depth and width (a), Inconel 625 track cross-section area from (b), Al7050 (c).

A good agreement has been found except for width values for deep keyhole shapes. The typical keyhole cross-section geometry is characterised by a width profile rapidly changing from wide, near the surface, to narrow deep below. The simplified approach of the present model is not capable to catch this geometry complexity. The net result is that it fails in giving precise width values, although the calculated depth and cross-sectional area fit well the measured values.

The fitting parameters: h and α shows the trends against specific energy,

shown respectively in Figure 2 and Figure 3.

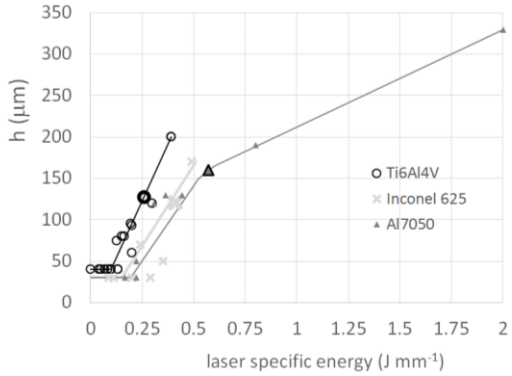

Fig. 2. Calculated trends of height *h* vs specific energy for the three analysed alloys.

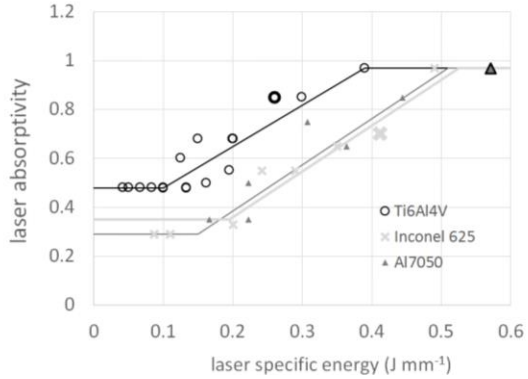

Fig. 2. Calculated trends of laser absorptivity vs specific energy for the three analysed alloys.

Bold symbols in Figure 2 and 3 highlight specific energies above which deep keyhole is experimentally observed for the three alloys. Dilip et al. [28] put into evidence the presence of keyhole porosity for specific energies above 0.26 J mm^{-1}. Montgomery et al. [27] notice keyhole shape for specific energies above 0.4 J mm^{-1} and Qi et al. [29] recognise well-developed keyhole regime only at very high power level, close to 2 J mm^{-1}, although severe keyholing is detected at specific energy as low as 0.57 J mm^{-1}.

While for Ti6Al4V and Inconel 625 this experimental outcome meets the respective calculated curves at $\alpha \approx 0.8$, the keyhole observed in Al7050 tracks appears for a calculated $\alpha = 0.97$.

CONCLUSION

A model has been developed using the commercial code ANSYS Fluent for simulating the printing process inside an L-PBF machine. A simplified approach has been adopted to make the model use as much practical as possible for design the processing window of alloys of any composition.

The model has been calibrated fitting experimental measures of track width, depth and cross-sectional area taken from three literature sources, referring to Ti6Al4V, Inconel 625 and Al7050.

A strategy of model calibration is employed based on varying the effective liquid pool thermal conductivity to fit the experimentally observed evaporation start with the calculation of the boiling temperature as maximum pool temperature. Laser absorptivity and depth of application of laser energy are further varied to fit width and depth data. They result to rise almost linearly with increasing specific energy assuming slopes very close for the three analyzed alloys. In particular, laser absorptivity increase from the base level consistent with the absorptivity of the alloy at the laser wavelength, until reaching a maximum value close to unity. From the experiments described in the reference papers used in this work, deep keyhole already appears for calculated values of absorptivity of almost 0.8.

The model needs to be further calibrated to validate the present observations and refine the fitting parameters (effective liquid conductivity, the slope of h and □).

REFERENCES

1. P. Petrousek et al.: Acta Metallurgica Slovaca, 25, 2019, 283-290. DOI: 10.12776/ams.v25i4.1366
2. L. Parilak, E. Dudrova, R. Bidulsky, M. Kabatova: Powder Technology, 322, 2017, 447. DOI: 10.1016/j.powtec.2017.09.027
3. D. Manfredi, R. Bidulsky: Acta Metallurgica Slovaca, 23(3), 2017, 276-282. DOI: 10.12776/ams.v23i3.988.
4. A. Di Schino, L. Valentini, J.M. Kenny, Y. Gerbig, I. Ahmed, H. Haefke: Surf. Coat. Technol., 161, 2002, 224-231. DOI: 10.1016/S0257-8972(02)00557-1.
5. G. Bregliozzi, A. Di Schino, J.M. Kenny, H. Haefke: Materials Letters, 57, 2003, 4505-4508. DOI: 10.1016/S0167-577X(03)00351-3
6. G. Napoli, M. Paura, T. Vela, A. Di Schino, Metalurgija, 57, 2011, 111-113.
7. R. Bidulsky et al.: Acta Physica Polonica A, 128(4), 2015, 647-650. DOI: 10.12693/APhysPolA.128.647
8. H.W. Mindt, O. Desmaison, M. Megahed, A. Peralta, J. Neumann: Journal of Materials Engineering and Performance, 27, 2018, 23-43. DOI: 10.1007/s11665-017-2874-5
9. H. Gong, K. Rafi, H. Gu, T. Stucker: Additive Manufacturing, 2014, 1-4, 87-98. DOI: 10.1038/s41598-019-54293-w
10. S. Khairallah, A. Anderson, T. Wayne, R. King: Acta Materialia, 108, 2016, 36-45. DOI: 10.1016/j.actamat.2016.05.017
11. C Zitelli, P. Folgarait, A. Di Schino: Metals, vol. 9, 2019, 731. DOI: 10.3390/met9070731.
12. A. Di Schino, P.E. Di Nunzio: Acta Metallurgica Slovaca, 23, 2017, 62-71. DOI: 10.12776/ams.v23i1.852.
13. R. Bidulsky, M. Actis Grande, E. Dudrova, M. Kabatova, J. Bidulska: Powder Metallurgy, 59(2), 2016, 121-127. DOI: 10.1179/1743290115Y.0000000022.
14. A. Di Schino, M. Longobardo, G. Porcu. G. Turconi, L. Scoppio: NACE – International Conference Series 2006, 062151-06125114.
15. A. Di Schino: Acta Metallurgica Slovaca, 22, 2016, 266-270. DOI: 10.12776/ams.v22i4.815
16. A. Di Schino, P. Di Nunzio. G.L. Turconi, Materials Science Forum, 558-559, 2007, 1435-1441. DOI: 10.4028/0-87849-443-x.1435.
17. G. Bregliozzi, S.I.U. Ahmed, A. Di Schino, K.M. Kenny, H. Haefke: Tribol. Lett., vol. 17, 2004, 697-704.
18. J. Bidulska, T. Kvackaj, I. Pokorny, R. Bidulsky, M. A. Grande: Archives of Metallurgy and Materials, 58, 2013, 371-375. DOI: 10.2478/amm-2013-0002
19. J. Bidulska, R. Bidulsky, T. Kvackaj, M. A. Grande: Materials, 12, 2019, 3724. DOI: 10.3390/ma12223724.
20. D. Almangour, D. Grzesiak, J. Cheng, Y. Ertas: Journal of Materials Processing Technologies, 257, 2018, 288-301- DOI:1 0.1016/j.jmatprotec.2018.01.028

21. T. Bartel, I. Guscke, A. Menzel: Computer and Mathematic with applications, 78, 2019, 2267-2281 DOI:10.1016/j.camwa.2018.08.032
22. M. Schanzel, D Shakirow, A. Ilin, V. Ploshikhin: Computer and Mathematic with applications, 78, 2019, 2230-22461 DOI:10.1016/j.camwa.2018.01.019.
23. J. Beuth, N. Klingbeil: JOM, 53, 2001, 36-39.
24. R. Rufini, O. Di Pietro, A. Di Schino: Metals, 8, 2018, 519. DOI: 10.3390/met8070519.
25. A. Di Schino, J.M. Kenny, G. Abbruzzese: J. Mater. Sci., 37, 2002, 5291-5298. DOI: 10.1023/A:1021068806598.
26. A. Di Schino, J.M. Kenny, I. Salvatori, G. Abbruzzese: J. Mater. Sci., 36, 2001, 593-601. DOI: 10.1023/A:1004856001632.
27. C. Montgomery, J. Beuth, L. Sheridan, N. Klingbeil: Proceedings of the Annual International Solid Freeform Fabrication Symposium, 2015, 1195–1204.
28. J. Dilip, S. Zhang, C. Teng, K. Zeng, C, Robinson, D. Pal, B, Stucker: Progress in Additive Manufacturing, 2, 2017, 157–167. DOI: 10.1007/s40964-017-0030-2
29. T. Qi, H. Zhu, H. Zhang, J. Yin, L. Ke, X. Zeng: Materials & Design, 2017. DOI: 10.1016/j.matdes.2017.09.014.
30. W. King, H. Barth, V. Castillo, G. Gallegos, J. Gibbs, D. Hahn, C. Kamath, A. Rubenchik: Journal of Materials Processing Technology, 214, 2014, 2915–2925.
31. M. Maina, R. Okamoto, R. Inoue, S. Nakashiba, A. Okada, T. Sakagawa,: Appl. Sci., 8, 2018, 1-13. DOI: 10.3390/app8122364
32. T. Mukherjee, J. Zuback, S. De, T. DebRoy, 7th International Symposium on High-Temperature Metallurgical Processing, 2016, 471-478.
33. L. Viet, J. Hye-Jin: Metals, 8, 2018, 815. DOI: 10.3390/met8100815
34. M. Ridolfi, P. Folgarait, V. Battaglia, T. Vela, D. Corapi, A. Di Schino: Procedia Structural Integrity, 24, 2019, 370-380. DOI: 10.1016/j.prostr.2020.02.034

OPEN ACCESS

ACTA METALLURGICA SLOVACA

2020, VOL. 26, NO. 1, 11-16

RESEARCH PAPER

Investigation of the effect of isothermal heat treatments on mechanical properties of thermo-mechanically rolled S700MC steel grade

Serkan Oktay [1], Paolo Emilio Di Nunzio [2], Mustafa Kelami Şeşen [1]*

[1] ***Istanbul Technical University, Istanbul, Turkey***

[2] ***RINA Consulting - Centro Sviluppo Materiali S.p.A., Rome, Italy***

*Corresponding author: paolo.dinunzio@rina.org; Centro Sviluppo Materiali, Rome, Rome, Lazio 00128, Italy

Received: 20.01.2020
Accepted: 18.03.2020

ABSTRACT

The effect of isothermal heat treatments (1 hour at 200, 400, 600 and 800°C) on mechanical properties of thermo-mechanically rolled S700MC steel has been investigated by extensive mechanical characterizations. Treatments at 600°C increase yield and tensile strength and decrease impact energy. Below 600°C the steel retains its bainitic structure. Simulations of precipitation kinetics suggest that this hardening effect arises from the nucleation of fine (Ti,Nb)C particles, indicating that the bainitic structure is unstable above 600°C due to its high supersaturation with respect to C, Nb and Ti. These results can help to optimize the operating practices for post-weld heat treatments.

Keywords: High Strength Steels, TMCP, thermal treatment, S700MC

INTRODUCTION

In the last years the industrial demand for high strength steels (HSS) with increasing mechanical performance to reduce the overall weight of the components, has stimulated the steel producers to develop and commercialize many steel grades capable of reaching a strength up to 1 GPa and even more [1].
The industrial route for producing these materials makes use of the so-called thermo-mechanical control process (TMCP) which exploits the austenite grain refining properties of Nb as microalloying element, together with a proper design of the hot rolling schedule, to improve the homogeneity of the microstructure and enhancing the mechanical properties in the as-hot rolled state. The corresponding refinement of the final microstructure after phase transformation on the run-out table permits to employ leaner chemical compositions thus reducing the production costs and casting problems. Moreover, less alloyed compositions have a lower carbon equivalent which makes easier all the joining operations to build up the final component, such as conventional arc welding processes as well as hybrid techniques.
Among the most performing high strength grades, S700MC is largely employed since its high tensile properties are associated to a good toughness.
To achieve the grade it is necessary to obtain a bainite + ferrite or a fully bainitic microstructure together with a controlled level of alloying elements.
Ferrite-bainite steels have a high tensile strength and both an adequate elongation and excellent hole expansion performance which ensures good formability. Fully bainitic high strength steels can be employed in the automotive industry to produce structural components for passenger safety such as anti-intrusion frames [2, 3] as well as in applications where wear resistance is required, such as components of industrial vehicles and trucks.
There are two main routes for producing this grade as hot rolled strip. In the first one, the required level of hardenability is achieved by a proper alloying with Mo, Cr and Mn. In the second one the addition of boron is exploited to induce the necessary hardenability to the austenite and permits to use a lower amount of alloying elements.
In some cases additional thermal treatments are employed to correct or improve the mechanical properties of as-rolled strips, especially of large thickness, also in-line with the hot rolling mill [4]. However, only few studies of the stability of bainitic structures and the evolution of the mechanical properties with the treatment temperature are available in the literature for this grade [5, 6].
In this work, the response to different isothermal heat treatments of a fully bainitic 5 mm thin strip of S700MC steel is investigated and analyzed.
Although the behavior of S700MC to welding is generally good due to its relatively low carbon equivalent [7-11], this study provides additional information on joining of this high strength steel, especially regarding the optimization of the operating practices for post-weld heat treatments when they are required to reduce hardness peaks in the heat affected zone caused by the joint geometry or by a not adequate selection of the welding conditions.

MATERIAL AND METHODS

Slabs of the S700MC steel grade have been produced by electric arc furnace (EAF) route. The chemical composition of the steel, reported in Table 1, complies with the DIN EN 10149 2 reference. The fully bainitic microstructure of the as-hot rolled material is obtained without boron additions. After reheating at 1230±20°C, slabs are thermo-mechanically hot rolled from 220 mm to 5 mm thickness with a finish roughing temperature between 1050 and 1100°C, a finish rolling temperature of 860 ±20°C (the calculated Ae_3 temperature is about 825°C) and a coiling temperature of 450 ± 20°C.

Table 1. Chemical composition of the hot rolled strip (mass %) and tensile properties of the S700MC steel grade according to the DIN EN 10149-2 reference standard for a strip thickness between 3 and 8 mm.

C	Mn	Si	P	S	Cr	Mo
0.09	1.9	0.19	0.015	0.003	0.22	0.14
Nb	V	Ti	N	Ni	Cu	Al
0.069	0.04	0.10	0.006	0.11	0.2	0.036

Re_H (MPa)	Rm (MPa)	Elongation (%)
≥ 700	750 - 950	> 12

Some thermodynamic and kinetic calculations, performed by the *JMatPro*® [12] commercial software, are here reported to characterize the behavior of the S700MC steel grade with respect to phase transformations and precipitation of Nb and Ti carbonitrides. In this formulation of the S700MC grade titanium microalloying is used to control the austenite grain size during slab reheating in order to avoid abnormal grain growth and inhomogeneous starting microstructures in the slab that might impair the product quality [13]. The first aspect considered is the precipitation in austenite of carbonitrides of the microalloying elements Nb and Ti as a function of temperature, with particular reference to the interval from 1300 to 850°C where the hot rolling is carried out. Although carbonitrides are crystallographically isomorphous and mutually miscible, two distinct phases have been considered. They have been schematically denoted as (Ti,Nb)(C,N) and (Ti,Nb)C to mean the high- and low-temperature stable phases, the former being rich in Ti and N, the latter in Nb and C. Typically, the first one is representative of the coarse precipitation (about 1 μm average size) produced from casting down to slab reheating. Its calculated composition is $(Ti_{0.95},Nb_{0.05})(C_{0.7},N_{0.3})$. The second one, finer, is typical of the hot deformation hand its calculated composition is $(Ti_{0.55},Nb_{0.45})C$. The evolution of

their mole fraction with temperature is shown in Figure 1. (Ti,Nb)(C,N) starts forming at about 1500°C whereas the precipitation start of the Nb-rich phase occurs at a temperature close to the roughing of the slab (about 1100°C) and increases as temperature decreases.
As far as the austenite decomposition is concerned, a continuous cooling transformation (CCT) diagram has been calculated from the finishing rolling temperature (850°C) assuming an austenite grain size of 10 µm. The curves in Figure 2 refer to a transformed fraction of 5%. It can be observed that the critical cooling rate for avoiding the ferrite nose is about 40°C/s in the range 650-550°C and it can be easily achieved on the run-out table of a hot strip mill for a 5 mm thin strip. Coiling at 450°C prevents the formation of martensite, being the Ms temperature for this steel about 425°C and the bainite start Bs about 590°C.

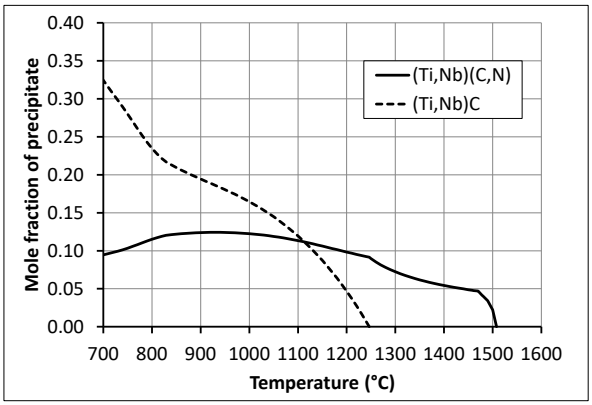

Fig. 1 Calculated equilibrium mole fraction of Nb and Ti carbonitrides in the S700MC steel as a function of temperature.

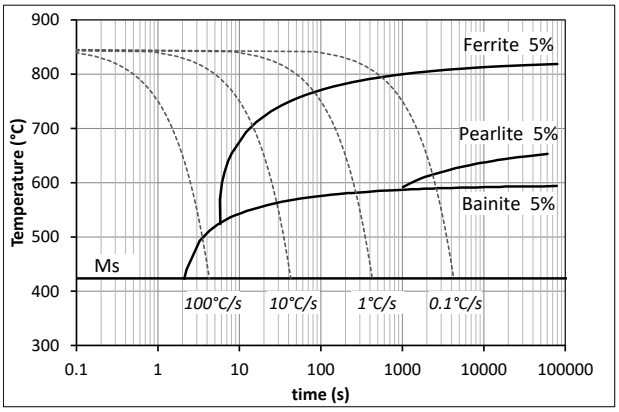

Fig. 2 Calculated CCT diagram of the S700MC steel austenitized at 850°C with an average austenite grain size of 10 µm. Lines refer to 5% transformed volume.

Specimens for tensile, impact and bending tests and for microstructural examinations have been taken from the coil tail. Isothermal heat treatments have been carried out in a laboratory furnace for 1 hour at 200, 400, 600 and 800°C followed by free cooling in air. The as-rolled material has been used as reference.
Tensile tests have been carried out on a Zwick Z600 device with 600 kN maximum load capacity. Charpy impact tests have been performed by a Zwick RKP-450 device with 450 J maximum impact force. Bending tests have been performed by a DYZ-200 device.
Microstructural examinations of the samples have been carried out by a Nikon MA200 optical microscope with Clemex Image Analyzer System and by a Field Emission Gun Scanning Electron Microscope (FEG-SEM) Zeiss Sigma 300 equipped with Energy Dispersive X-ray Spectrometry (EDS) for microanalysis.

RESULTS

Tensile tests

Tensile tests have been carried out on flat test specimens according to the ASTM E8 reference standard (gauge length 50 mm). The results of tensile tests in the longitudinal direction are reported in Figure 3a. No relevant changes compared to the as-hot rolled condition are observed up to a holding temperature of 400°C. In this range the material still meets the standard requirements for the S700MC grade. A sharp increase in yield and tensile strength is observed for the holding temperature of 600°C where the highest values are obtained with an increase with respect to the as-rolled condition of about 80 MPa and 55 MPa, respectively. The sample treated at 800°C shows the lowest yield strength and a tensile strength substantially equivalent to the as-rolled reference state. Total elongation appears not affected by the treatments and the observed fluctuations can be considered within the scatter of the experimental determinations (Figure 3b).

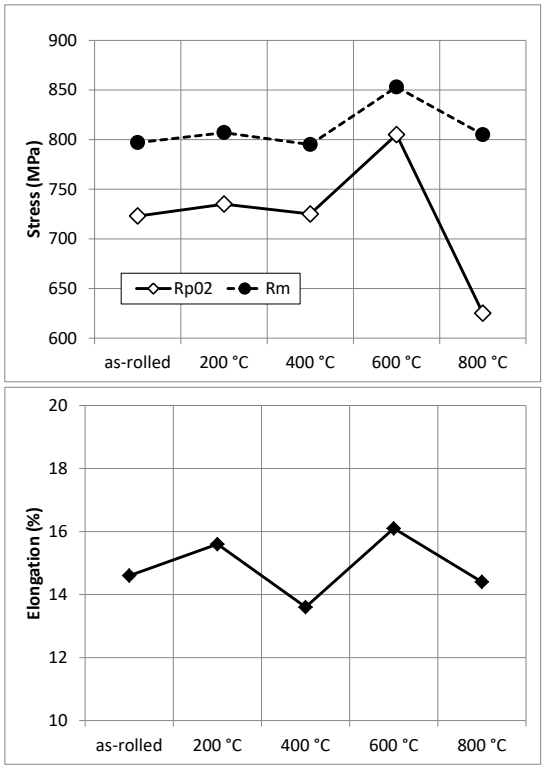

Fig. 3 Results of tensile test in longitudinal direction for the S700MC steel in the as-rolled condition and after isothermal heat treatment of 1 hour at different temperatures. a) Rp02 and Rm; b) Total Elongation.

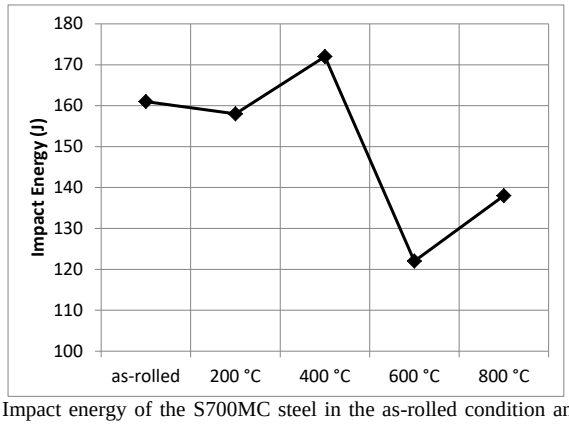

Fig. 4 Impact energy of the S700MC steel in the as-rolled condition and after isothermal heat treatment of 1 hour at different temperatures.

Impact and bending tests

Charpy V-notch impact tests have been carried out at room temperature on samples taken in the longitudinal direction. The test results are shown in

Figure 4. Up to the holding temperature of 400°C the impact energy is in the range of 155–175 J. A drop is observed for the treatment at 600°C. A further increase in the holding temperature to 800°C produces a partial recovery of the toughness level.
Fracture surfaces after the impact test are shown in Figure 5. Ductile fracture is the dominant mechanism for all the samples. Delaminations are particularly evident in the sample treated at 600°C.
Finally, bending tests have been carried out on samples in the transverse direction. The images of bent specimens are shown in Figure 6. In all cases the surfaces are defect-free.

Microstructure

Metallographic sections in transverse direction observed by optical microscope after etching with a Nital 2% solution are reported in Figure 7.

The microstructure of the sample treated at 200°C is fully bainitic and very similar to that of the as-rolled material. For a treatment at 400°C only small changes are observed. Instead, by increasing the holding temperature at 600°C the rolling structure undergoes an apparent rearrangement due to recovery with the partial recrystallization of bainite. In fact, ferrite grains appear slightly coarser and more equiaxed than those in the samples treated at lower temperatures. In addition, the reduction of the carbon supersaturation in ferrite promotes the observed coarsening of grain boundary carbides. Finally, the microstructure of the specimen treated in the intercritical region is reverted to a ferrite-pearlite mixture. Large (Ti,Nb)(C,N) precipitates formed at high temperature with size in the range 3 to 5 μm are evidenced in the pictures.

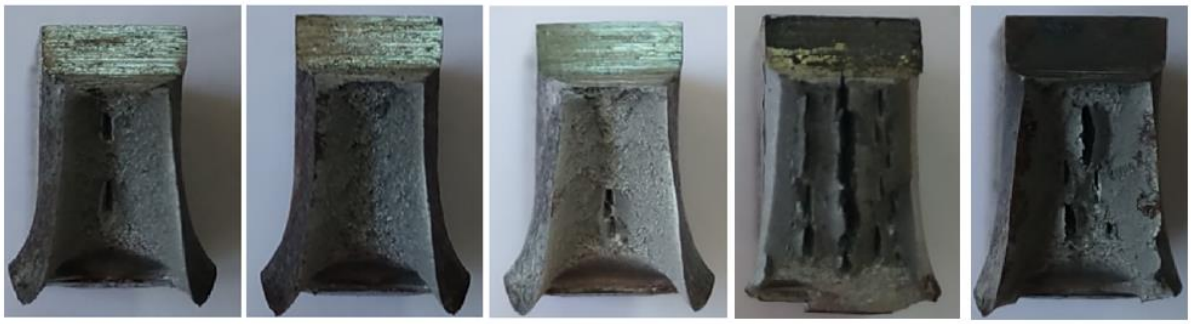

as-rolled 200°C 400°C 600°C 800°C

Fig. 5 Appearance of the fracture surfaces of S700MC steel grade as-rolled and isothermal heat treated at different temperatures after impact tests.

as-rolled 200°C 400°C 600°C 800°C

Fig. 6 Appearance of the bent surfaces of the S700MC steel grade as-rolled and isothermal heat treated at different temperatures after the bending tests.

SEM and microanalytical EDS investigations have been carried out on all samples. For the sake of clarity, only the results of the specimens in the as-rolled condition and after 1 hour at 600°C are reported and discussed. In-Lens and secondary electron images of the selected samples are shown in Figure 8.
The bainitic structure of the as-rolled material is characterized by a relatively small grain size with a sub-grain structure (with average size of about 1.5 μm) and many inter-lath cementite particles. The material treated at 600°C has a larger and slightly more equiaxed structure of the ferrite grains with less sub-grains and cementite particles located at grain boundaries.
In both cases the smallest precipitates detected have an average size of about 200 nm and have been identified as (Ti,Nb)C. Being already present in the as-hot rolled state, they have been formed during hot rolling of the strip and probably during roughing. Some examples are reported in Figure 9. No precipitates containing Mo or V have been found.
SEM images of the fracture surface of the selected impact test samples are shown in Figure 10. The as-rolled material is characterized by a ductile fracture. Dimples are associated to precipitates and inclusions. The sample treated at 600°C has a mixed fracture mode. Although the fracture surface is generally ductile, locally some crystalline regions can be found.

DISCUSSION

Microstructural changes

From the characterization of the mechanical properties and microstructures of the S700MC steel grade it is apparent that a treatment temperature of 600°C is critical since it induces a reduction of toughness (Figure 4) although it is associated with an increase in YS and, at a lower extent, also of UTS (Figure 3).
The microstructural changes can be explained invoking an intense recovery of the bainite structure with a reduction of the dislocation density, coarsening of inter-lath carbides and a rearrangement of the high-angle grain boundaries with a slight increase of the average ferrite grain size. In addition, the sub-grain structure is almost completely eliminated. These factors support the decrease of the impact energy.
On the other hand, notwithstanding the slightly coarser grain size, tensile properties, and in particular the yield stress, increase. Since from the SEM investigation no apparent new precipitation or coarsening of (Ti,Nb)C particles in the size range below 100 to 200 nm is observed, it has to be argued that nanoprecipitation of (Ti,Nb)C (not detectable by the SEM) is produced in the matrix. As a matter of fact, as indicated by the thermodynamic calculations, in the as-rolled material, some niobium and titanium are still in solid solution together with some carbon due to the low coiling temperature of the hot strip and

to the formation of a bainitic microstructure composed by carbon-supersaturated bainitic ferrite laths.

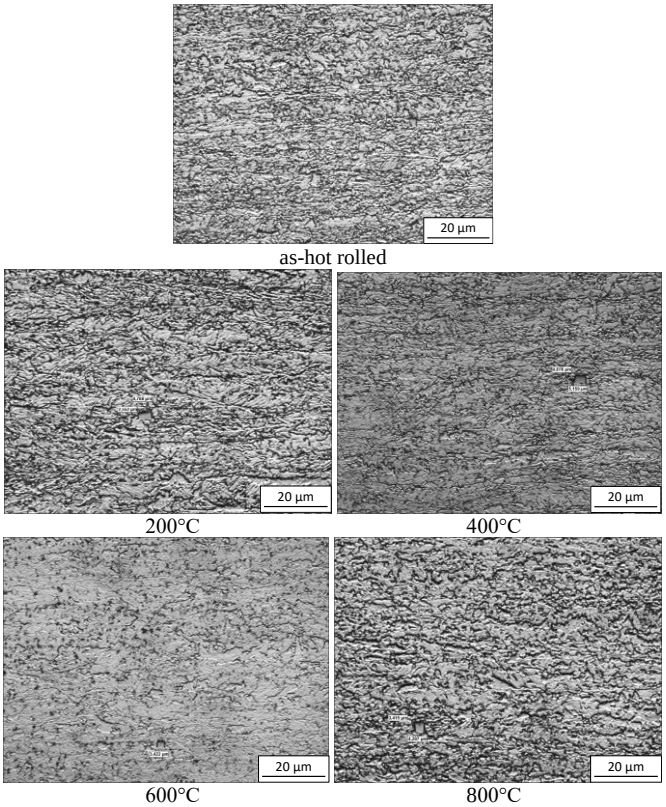

Fig. 7 Microstructure of the as-rolled and isothermal heat-treated S700MC steel (2% Nital etching, transverse direction).

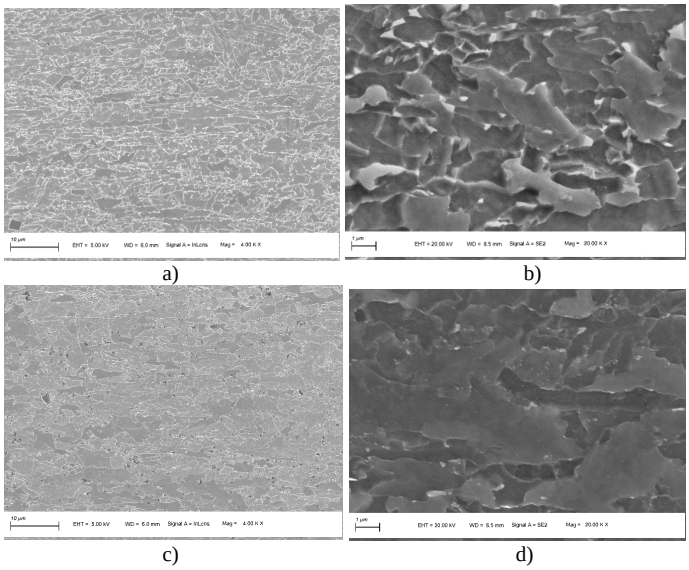

Fig. 8 In-lens SEM images of as hot rolled (a, b) and isothermally heat treated at 600°C for 1 hour (c, d) S700MC steel samples.

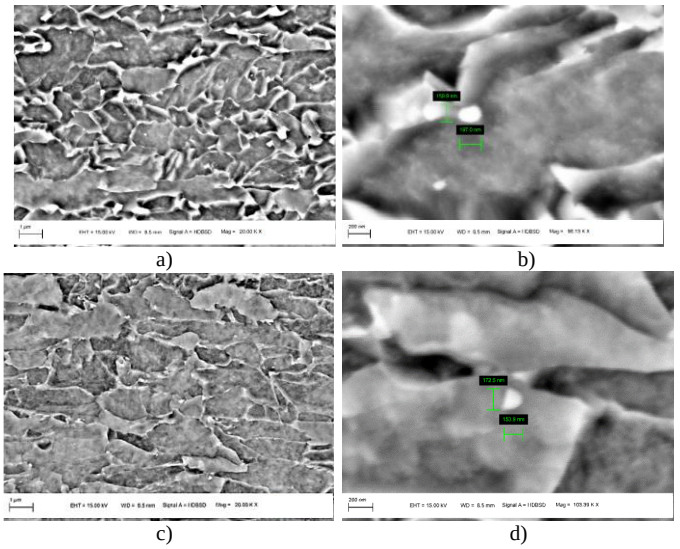

Fig. 9 Microstructure of S700MC steel (backscattered electrons) and details of typical (Ti,Nb)C precipitates in the as hot rolled state (a, b) and after isothermal heat treatment at 600°C for 1 hour (c, d).

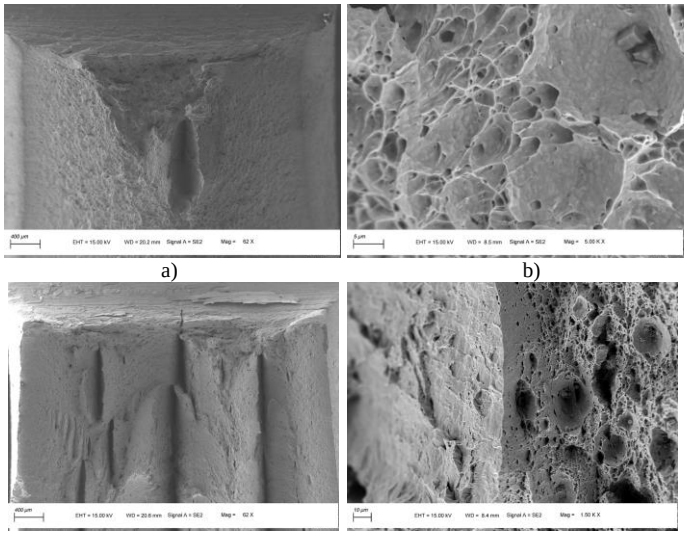

Fig. 10 SEM images of the fracture surface of selected impact test samples of S700MC steel strip: (a, b) as hot rolled; (c, d); isothermally heat treated 1 hour at 600°C.

In order to ascertain if this mechanism can be effective in explaining the above results, some calculations have been carried out using the commercial software *MatCalc* [14-19] which is able to simulate not only the thermodynamic equilibria but also the kinetics of nucleation and growth of precipitates in multicomponent systems. Calculations have been performed with the version 5.42 of the software using the databases mc_fe_v2.017.tdb for thermodynamic data and dmc_fe_v2.001.ddb for diffusion and mobility data.

Isothermal treatments of 1 hour at 400 and 600°C have been simulated considering the nucleation of (Ti,Nb)C particles on the grain boundaries of a bainitic ferrite matrix. In order to estimate the effect of hot rolling and coiling in determining the maximum amount of second phase that can be formed, the thermodynamic equilibrium composition of austenite at the roughing temperature (taken for the sake of simplicity equal to 1100°C) has been assumed as initial condition. At this stage, most of nitrogen is precipitated in coarse (Ti,Nb)(C,N) particles and the corresponding elements involved do not take part any more to

the subsequent precipitation processes. Furthermore, it has been reasonably assumed that a negligible precipitation occurs after roughing due to the short time of the hot rolling finishing treatment and to the low coiling temperature (about 450°C). By assuming an average grain size of the bainitic ferrite plate of 2 μm with a grain elongation factor of 2 and a dislocation density of 10^{12} m^{-2}, the calculation yielded a precipitate volume fraction of about $7 \cdot 10^{-5}$ and an average particle size of about 10 nm. After 1 hour of treatment the amount of Nb in solution is reduced of about 50% with respect to the initial condition and that of Ti of about 30%. Moreover, the calculations confirm that the same treatment at 400°C is not sufficient to activate the nucleation process, as observed in the experiments.

In order to estimate the strengthening effect produced by the fine precipitates after 1 hour at 600°C, the Ashby-Orowan equation [20] has been used

$$\Delta\sigma_{Y\ ppt}\,[MPa] = 10.8 \cdot \frac{\sqrt{f_V}}{d} \cdot ln\left(\frac{d}{6.25 \cdot 10^{-4}}\right) \quad , \qquad (1.)$$

where d is the average particle size (μm) and f_V the volume fraction of second phase. The *MatCalc* simulation results at 600°C permit to estimate a precipitation strengthening between 25 and 30 MPa, corresponding to about 50% of that measured at this temperature (Figure 3a). The remaining contributions, not explained by the present simulations, come presumably from precipitation of the supersaturated carbon as epsilon carbide in the bainitic ferrite. Also an ageing mechanism could be invoked which could explain the more pronounced increase of YS compared to UTS.

It has to be noticed that, although vanadium has been included in the kinetic calculations since, being miscible in the Ti-Nb carbonitrides, it can contribute to the precipitate volume fraction, nevertheless it does not enter the particles due to the too short annealing time not permitting a complete precipitation of solutes.

Annealing temperatures greater or equal to 800°C, implying a partial or full transformation in austenite (the calculated Ae_3 temperature for the present steel composition is about 825°C), annihilate the bainitic structure and dissolve all cementite precipitates (Figure 7). Even (Ti,Nb)C particles can be dissolved if temperature is high enough. Thus, after the slow cooling to room temperature, the steel recovers a structure composed of a mixture of ferrite and pearlite which is characterized by a much lower yield stress than the as-rolled material (Figure 3a). It has to be remarked that, unlike the treatments investigated by Sas *et al.* [21], in the present case there is neither hot deformation in the two-phase region nor a fast cooling. Consequently, the mechanical properties are not enhanced.

The above results permit to conclude that, due to the high level of residual supersaturation of the bainitic microstructure of the S700MC steel in the as-rolled state with respect to the precipitation of carbides of iron and microalloying elements, any thermal treatment carried out at a temperature high enough to activate the diffusion of interstitial elements has a relevant impact on the mechanical properties. In particular, a tempering temperature higher or equal to 600°C is particularly unfavorable since it induce a relevant secondary hardening effect and a reduction of toughness.

Welding issues

The present results can be exploited in relation to welding of the S700MC steel grade. For conventional welding techniques such as MAG, the commonly adopted procedures prescribe the use of low heat inputs, generally not exceeding 0.8 kJ/mm and typically around 0.4 kJ/mm [7-11] in order to prevent an excessive hardness in the heat affected zone (HAZ). Some welding simulations have been carried out by the CSMWeld model [22-25], a physical-semiempirical model developed at RINA-CSM which predicts the hardness in the HAZ of multi-pass joints. Starting from the imposed welding conditions (number of passes, heat input and chemical composition of the base material) it makes use of different sub-models for the simulating the thermal evolution at each pass, the austenite grain coarsening in the HAZ and the austenite decomposition during cooling as a function of the distance from the fusion line.

The model has been used to estimate the possible formation of hardness peaks in the HAZ in case of standard and not-standard welding conditions. Calculations have indicated that, with an heat input of 0.8 kJ/mm, the maximum hardness expected in HAZ is about 330±20 HV_{10}, to be compared with a hardness in the base metal of about 280 HV_{10}. An example of a hardness profile calculated for a bead-on-plate weld is reported in Figure 11. Consequently, no specific weldability problems are expected for this steel grade, in accordance with the EN 15614-1 standard which, for this class of materials (steel group 2.2 according to ISO/TR 15608) sets 380 HV_{10} as upper limit of untreated HAZ.

Nevertheless, especially if the joint geometry is complex and in association with higher strip thickness, welding issues can arise. In these specific cases, a post-weld heat treatment might be necessary to reduce the hardness peaks. Consequently, it is important that the thermal treatments are performed below 600°C in order to avoid loss of toughness in the base metal close to the HAZ.

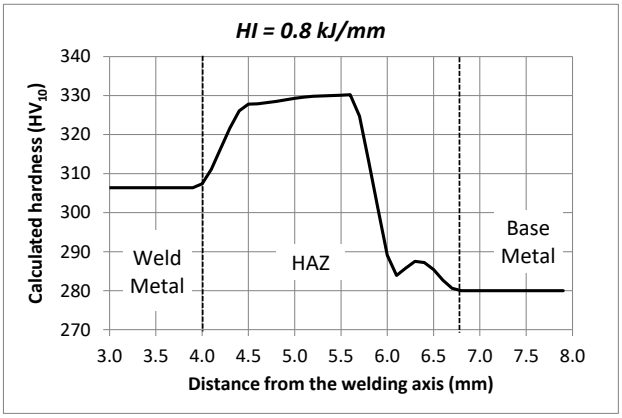

Fig. 11 Calculated hardness profile in HAZ for a bead-on-plate weld of S700MC with a heat input of 0.8 kJ/mm.

CONCLUSION

This study on the behavior of the bainitic HS steel grade S700MC subjected to isothermal treatments of 1 hour at temperatures in the range 200-800°C has shown that temperatures greater or equal to 600°C, although improving the tensile properties of the material, produce a decrease of toughness, thus confirming previous results in the literature. It is here proposed that this hardening effect arises from the additional precipitation of fine particles of (Nb,Ti)C and epsilon carbides and ageing, thus indicating that the bainitic structure is unstable above 600°C due to its inherent high level of supersaturation with respect to C, Nb and Ti. In case of application of post-weld heat treatments of joints involving this steel grade, the above temperature should not be exceeded.

REFERENCES

[1] K.C. Agrawal Industrial Power Engineering and Applications Handbook, 1st ed.; Elsevier Inc, 2001.

[2] C. Mesplont, T. Waterschoot, S. Vandeputte, D. Vanderschueren, B.C. De Cooman, *Development of High-Strength Bainitic Steels for Automotive Applications*, 41st Mechanical working and steel processing conference proceedings, 1999, vol. 37, p. 515-524.

[3] Ö. Kaya, K. Çetinkaya, D. Çimen, Z. Çetin, B. Derin, *The Effect of Nitrogen-Containing Vanadium Alloying Element Additions on the Properties of S550MC Grade Steels*, Proc. 19th International Metallurgy & Materials Congress (IMMC) 2018, 789-792.

[4] Yu.I. Matrosov, O.P. Talanov, I.V. Lyasotskii, D.L. Dyakonov, E.I. Khlusova, V.V. Orlov, A.M. Korchagin, D.S. Tsvetkov, S.D. Popova, Metallurgist, 55, 2011, 489-495. https://doi.org/10.1007/s11015-011-9457-8.

[5] Yu.I. Matrosov, I.V. Ganoshenko, O.A. Bagnet, T.Yu. Ivanova, Stal', 2, 2005, 74–78.

[6] J. Górka, Advanced Materials Research, 1036, 2014, 111-116. doi:10.4028/www.scientific.net/AMR.1036.111.

[7] A. Silva, B. Szczucka-Lasota, T. Węgrzyn, A. Jurek, Welding Technology Review 91, 2019, 23-28 (https://doi.org/10.26629/wtr.v91i3.1043).

[8] J. Górka, IOSR Journal of Engineering 3, 2013, 22-28.

[9] J. Górka, *An influence of welding thermal cycles on properties and HAZ structure of S700MC steel treated using thermomechanical method*, Proc. IX International Congress "Machines, Technologies, Materials" 3, 2012, 41-44.
[10] J. Górka, International Journal of Engineering Science and Innovative Technology, 2, 2013, 383-390.
[11] J. Górka, Indian Journal of Engineering and Materials Science, 22, 2015, 497-502.
[12] N. Saunders, Z. Guo, X. Li, A.P. Miodownik, J.-Ph. Schillé, *Using JMatPro to Model Materials Properties and Behavior*, Journal of Metals, 2003, 60-65. DOI:10.1007/s11837-003-0013-2.
[13] T. Kvačkaj, L. Nemethova, R. Misicko, I. Pokorny, High Temp. Mater. Proc. 30, 2011, 535–538. DOI 10.1515/HTMP.2011.110.
[14] E. Kozeschnik, *Modeling Solid-State Precipitation*, Momentum Press, LLC, ISBN 978-1-60650-062-0, 2013, 464 pages. (https://www.matcalc.at/)
[15] E. Kozeschnik, J. Svoboda, R. Radis, F.D. Fischer, Modelling and Simulation in Matererials Science and Engineering 18, 2010, 015011 (19 pages) https://doi.org/10.1088/0965-0393/18/1/015011.
[16] E. Kozeschnik, J. Svoboda, F. D. Fischer, CALPHAD 28 (4), 2005, 379-382. https://doi.org/10.1016/j.calphad.2004.11.003.
[17] J. Svoboda, F.D. Fischer, P. Fratzl, E. Kozeschnik, Materials Science and Engineering A, 2004, 385 (1-2) 166-174. https://doi.org/10.1016/j.msea.2004.06.018.
[18] M. Nöhrer, W. Mayer, S. Primig, S. Zamberger, E. Kozeschnik, H. Leitner, Metallurgical and Materials Transactions A, 45, 2014, 4210-4219. DOI: 10.1007/s11661-014-2373-3.
[19] S. Zamberger, T. Wojcik, J. Klarner, G. Klösch, H. Schifferl, E. Kozeschnik, Steel Res. Int. 84, 2013, 20-30. https://doi.org/10.1002/srin.201200047.
[20] T. Gladman, *The physical metallurgy of microalloyed steels*, the Institute of Materials, Cambridge University Press, Cambridge, 1997.
[21] J. Sas, T. Kvačkaj, O. Milkovič, M. Zemko, 9(12), 2016, 971 (8 pages). doi:10.3390/ma9120971.
[22] P.E. Di Nunzio, M. Monti, V. Picozzi, *CSMWELD: a model predicting hardness and microstructure of multipass welds of C-Mn and microalloyed steels* 16° Congresso AIPnD, (National conferene on non-destructive testing, monitoring and diagnostics), Milan, Italy, October 2015.
[23] P.E. Di Nunzio M.C. Cesile, E. Anelli, G. Richard, *Prediction of microstructure and hardness of multipass heat affected zone in high strength steel girth welds* Int. Conf. “New Developments on Metallurgy and Application of High Strength Steels, Buenos Aires 2008”, Buenos Aires, May 26-28 2008, TMS 2008, 597-610.
[24] P.E. Di Nunzio, M.C. Cesile, E. Anelli, A. Poli, *A physical model for microstructural predictions in multi-pass welding of seamless pipes*, Proc. Materials Solutions Conference 2002 - International Symposium on Microalloyed Steels, ed. by R.I. Asfahani, R.L. Bodnar, M.J. Meerwin, 7-9 October 2002, Columbus, OH, ASM Int., Materials Park, OH, September 2002, 148-156.
[25] E. Anelli, M.C. Cesile, P.E. Di Nunzio, G. Cumino, M. Tivelli, A. Izquierdo, *Application of metallurgical modeling to multi-pass girth welding of seamless linepipes*, International Conference on the Application and Evaluation of High-Grade Linepipes in Hostile Environments (Pipe Dreamer Conference), Girth welding (III) Session, Yokohama, JAPAN November 7-8, 2002.

OPEN ACCESS

ACTA METALLURGICA SLOVACA

2020, VOL. 26, NO. 1, 17-23

RESEARCH PAPER

INFLUENCE OF A POLYCARBOXYLATE BASED SOLUTION ON STABILITY OF HYDROGEN PEROXIDE AND APPLICATION TO E-WASTE LEACHING

*Ersin Y. YAZICI**

Hydromet B&PM Research Group, Div. of Mineral&Coal Processing, Dept. of Mining Eng., Karadeniz Technical University (KTU), Trabzon, Turkey

**Corresponding author: eyazici@ktu.edu.tr; tel.: +904623773683, Hydromet B&PM Research Group, Div. of Mineral&Coal Processing, Dept. of Mining Eng., Karadeniz Technical University (KTU), Trabzon, 61080, Turkey*

Received: 20.11.2019
Accepted: 22.12.2019

ABSTRACT

Hydrogen peroxide with its high oxidising potential is commonly used in hydrometallurgical extraction of metals from ores, anode slimes and waste materials (e.g. WEEE) and treatment of cyanidation effluents. Main detraction to H_2O_2 is its rapid catalytic decomposition leading to prohibitively high consumption. Effect of pH (0-4), Cu(II) (0-10 g.l^{-1}) and temperature (20-80°C) on H_2O_2 stability was investigated using response surface methodology. Influence of neutral-alkaline conditions (pH 7.3-11.8) and presence of solids (1-20% w/v) was also tested. A polycarboxylate based solution (PBS) was utilised to improve H_2O_2 stabilisation. The significance order of parameters on H_2O_2 decomposition was temperature > pH > Cu(II). Elevating the level of these parameters increased H_2O_2 decomposition. The activation energy (60.7±2.5 kJ.mol^{-1}) indicated a chemically controlled process. Alkaline conditions (up to pH 11.8) led to higher H_2O_2 decomposition. Presence of solids adversely affected H_2O_2 stability under certain conditions. The addition of PBS significantly improved (up to 54%) H_2O_2 stability in the presence of copper. The presence of PBS in H_2SO_4-H_2O_2 leaching of waste of printed circuit boards (WPCBs) provided a limited enhancement in copper extraction by up to 19%. PBS can be suitably utilised to stabilise and hence reduce H_2O_2 consumption in aqueous solutions particularly in the presence of copper.

Keywords: Hydrogen peroxide; polycarboxylates; stabilization; copper; e-waste; leaching

INTRODUCTION

Hydrogen peroxide (H_2O_2) has been employed in many industrial applications due to its superior features including high oxidation potential (+1.78 V) [1], easy handling-storage and environmentally friendly nature i.e. formation of no toxic by-products during the oxidation process (Eq. 1) [2,3]. Hydrogen peroxide is extensively used in hydrometallurgical applications including leaching of gold/silver from ores to increase dissolved oxygen concentration [3,4], extraction of copper from chalcopyrite ores/concentrates as well as waste materials (e.g. WEEE) in acidic sulphate/chloride solutions under atmospheric or oxidative conditions [5-10], extraction of precious metals from anode slimes by chloride leaching [11] and precipitation of uranium and plutonium in peroxide form from pregnant leach solutions (PLSs) [12,13]. Hydrogen peroxide is also effectively used in chemical oxidation of cyanidation effluents containing free and weak acid dissociable (WAD) cyanides [14-17]. Notwithstanding this, application field of hydrogen peroxide includes waste treatment such as direct oxidation of inorganic (e.g. sulphide (S^{2-}), nitrite) and organic contaminants (e.g. formaldehyde, thiols) in drinking/natural water, oxidation of organics using advanced oxidation processes (AOP) (Fenton's process (Fe^{2+}/H_2O_2) or $H_2O_2/UV/O_3$) [3,18,19].

$$2H_2O_2 \rightarrow O_2 + 2H_2O \quad (1)$$

Despite its attributes, hydrogen peroxide is prone to catalytic decomposition resulting in increased reagent consumption, which may lead to an adverse effect on process economics [16]. For instance, in treatment of cyanide effluents (pH 10-11), despite the theoretical consumption of hydrogen peroxide for the oxidation of free cyanide is 1.31 g H_2O_2 per g CN^-, in practice, this increases by 1.5-6.1 fold [16]. Factors negatively influencing the stability of hydrogen peroxide include presence of metal ions (e.g. Fe^{3+}, Fe^{2+}, Mn, Cu^{2+} and Cr^{2+}) (Eqs. 2-3) [20-24], solids [25-26], sulphur ions (S^{2-}) (Eq. 4), thiocyanate (SCN^-) (Eq. 5) as well as the increase in temperature and pH [2,16,27]. Yazıcı and Deveci [27] demonstrated that in alkaline solutions (pH 9.5-12), increasing the concentration of copper as well as solids ratio, temperature and pH facilitate the decomposition of hydrogen peroxide.

$$2Cu^{2+} + H_2O_2 + 2OH^- \rightarrow 2Cu^+ + O_2 + 2H_2O \quad (2)$$
$$Fe^{2+} + H_2O_2 \rightarrow Fe^{3+} + OH^- + OH\bullet \quad (3)$$
$$S^{2-} + H_2O_2 \rightarrow S^0 + 2OH^- \quad (4)$$
$$SCN^- + H_2O_2 \rightarrow S^0 + OCN^- + H_2O \quad (5)$$

Various inorganic/organic additives appeared to be tested in the literature for inhibition of catalytic decomposition of hydrogen peroxide by metal ions, copper in particular [22,23,26,28-31]. Many of the relevant studies focused on the improvement of the stability of concentrated acidic (stock) solutions of hydrogen peroxide (25-90% w/w H_2O_2) in order to extend shelf life of H_2O_2 products, with limited details. To the author's knowledge, there is limited work on the practical use of organic/inorganic additives for inhibition of decomposition of hydrogen peroxide in acidic/basic solutions. In a previous study, Mahajan et al. [32] showed that the addition of ethylene glycol (1-8 ml.l^{-1}) enhanced leaching of copper from chalcopyrite in H_2SO_4-H_2O_2 solutions. Bas et al. [33] found that ethylene glycol can be suitably used as an additive in hydrogen peroxide treatment of X-ray film effluents (thiosulphate media) for silver recovery. More recently, Ruiz-Sánchez and Lapidus [34] addressed the beneficial use of ethylene glycol in the peroxide leaching of chalcopyrite mineral. The current study has been also the first attempt for improvement of copper extraction from e-waste through stabilisation of hydrogen peroxide in sulphuric acid leaching.

In this study, the effect of pH (0-4), the concentration of Cu(II) (0-10 g.l^{-1}) and temperature (20-80°C) on the decomposition of hydrogen peroxide were investigated using response surface methodology in five levels over a period of 3 h. The effects of high pHs (up to 11.8) and solids (1-20% w/v) were also tested separately. The influence of a polycarboxylate based solution (2.5-20 ml.l^{-1} PBS) as the additive on the stability of hydrogen peroxide was also tested in much detail i.e. under different conditions of pH, temperature and solids ratio. The effect of PBS (1.3-6.7 ml.l^{-1}) on copper extraction from a waste of printed circuit boards (WPCBs) was also demonstrated.

MATERIAL AND METHODS

Tests were performed in baffled jacketed glass reactors (inner dia: 6.5 cm, 250-mL nominal capacity) connected to a water circulator (Polyscience) for maintaining the desired temperature in reactors. A multi magnetic stirrer (Thermo Scientific Variomag) was used to agitate reactors using PTFE-coated magnetic bars (diameter: 3 cm) at a stirring speed of 350 rpm. The top of the reactors was kept covered with lids over the test period.

Hydrogen peroxide solution (35% w/w H_2O_2, Merck) and a stock solution of copper sulphate pentahydrate (200 g.l^{-1} $CuSO_4.5H_2O$) were used to prepare the

solutions in a final volume of 200 mL. Hydrogen peroxide was added after achieving the required temperature of the solution to prevent its decomposition before starting the test. The initial concentration of hydrogen peroxide was set at 0.5 M in all experiments. To test the effect of solids on the stability of hydrogen peroxide, quartz, which is an inert mineral (i.e. not soluble in acid/neutral/alkaline solutions) commonly present in ores, was selected. Quartz sample (>90% SiO_2, –250 µm) was firstly treated with a dilute acid solution (5% HCl, 60°C, 90 min.) to remove soluble impurities, followed by washing with distilled water. It was then dried in an oven (105°C) prior to use in the tests. A polycarboxylate based solution (PBS with a trade name of Polycar-100 produced by Iksa [35] (Table 1) was utilised as the additive to improve the stability of hydrogen peroxide. PBS is essentially a hyper plasticizer used to reduce water requirement in cement products [35]. The pH of the solutions was adjusted using either concentrated sulphuric acid solution (96%) or 4 M NaOH. All the solutions were prepared using deionised-distilled water. Samples taken at the predetermined intervals over a period of 180 min. (after centrifugation if solids were present to obtain clear supernatants) were analysed for initial and residual hydrogen peroxide with iodometric titration [36].

The addition of PBS (1.3-6.7 $ml.l^{-1}$) in hydrogen peroxide leaching copper from the waste of printed circuit boards (WPCBs, 18.5% Cu, 2.05% Fe) was also demonstrated. The details of the preparation of WPCBs sample can be found elsewhere [10]. Leach solutions (150 mL) containing 1 M H_2SO_4 + 1 M H_2O_2 were prepared in Erlenmeyer flasks (250 mL) prior to the addition of WPCBs sample (-250 µm) to maintain a solids ratio of 1% w/v. A temperature-controlled (80°C±1) reciprocal shaker operating at 140 rpm was used for mixing of the flask contents. Samples taken at certain intervals (i.e. 0.25 and 0.5 h) were centrifuged at 4100 rpm for 5 min. to collect supernatants for copper analysis using an atomic absorption spectrometer (Perkin Elmer AAnalyst 400). Initial and final pH, redox potentials ($E_{Ag/AgCl}$, mV) and hydrogen peroxide concentration were also monitored.

Table 1 Some properties of the polycarboxylate based solution (PBS)

Type	Mixture of polycarboxylate and organic salts
Colour	Light brown
Density	1.03 ± 0.02 $kg.l^{-1}$
pH	6.50-8.00
Alkali content	≤ 10%
Chloride	≤ 0.1%

Design of experiments and statistical analysis of data

Effect of various parameters including pH, the concentration of copper and temperature, on the decomposition rate of H_2O_2 was investigated using design of experiments i.e. central composite design (CCD), a type of response surface methodology (RSM) [37,38]. Table 2 shows the parameters and their corresponding levels. Design-Expert software [39] was used in the calculation of regression coefficients of second-order mathematical models produced, statistical analysis of experimental data and generation of response surface plots. P-values were used for testing the significance of parameters. Simply, the null hypothesis is rejected on the grounds that the P−value is under the selected confidence level (e.g. 95%, α=0.05). This indicates that the parameter tested is statistically significant [38]. Apart from experimental design runs, additional tests were also carried out to reveal the decomposition profile of hydrogen peroxide in neutral-alkaline conditions (i.e. pH 7.3-11.8) and in the presence of solids (i.e. 1-20% w/v). Furthermore, the effect of the PBS on the stability of hydrogen peroxide was investigated in detail under different experimental conditions.

Table 2 Parameters and corresponding levels tested in the decomposition of hydrogen peroxide

	Parameters	Levels				
		Lowest	**Low**	**Center**	**High**	**Highest**
		−1.682	**−1**	**0**	**+1**	**+1.682**
A	pH	0	0.8	2	3.2	4
B	Cu(II), $g.l^{-1}$	0	2	5	8	10
C	Temperature,°C	20	32	50	68	80

RESULTS AND DISCUSSION

Modelling and statistical analysis of data

The experimental design layout with conditions for each test and corresponding responses (i.e. decomposition of hydrogen peroxide (%) at different time intervals (5-180 min.) and initial rate constants (k, min^{-1})) is presented in Table 3. The relative standard deviation (RSD) of the experimental data was calculated to be ≤6.28%. The initial rate constants (k, min^{-1}) were calculated from the decomposition data (Table 3) using linear first-order model (Eq. 6) and also used as a response in the statistical evaluation of data (Table 3).

$$[H_2O_2] = [H_2O_2]_0 . e^{-k.t} \quad (6)$$

where; $[H_2O_2]$ - instant concentration (or decomposition ratio) of H_2O_2
$[H_2O_2]_0$ - initial concentration (or decomposition ratio) of H_2O_2
k - initial rate constant (min^{-1})
t - time (min.)

Table 3 Central composite design (CCD) with experimental conditions and corresponding results for decomposition rates (%) of H_2O_2 at different time intervals (5-180 min.) and initial rate constants (k, min^{-1}) ($[H_2O_2]_0$: 0.5 M)

No	pH	Cu(II) ($g.l^{-1}$)	Temp (°C)	Decomposition of H_2O_2 (%)								Rate constant, $k.10^3$ min^{-1}
				5min	15min	30min	60min	90min	120min	150min	180min	
1	0.8	2	32	1.77	1.77	1.77	1.77	1.77	1.77	1.77	1.77	1.02
2	3.2	2	32	4.76	4.76	4.76	9.74	9.74	12.2	14.7	22.1	1.08
3	0.8	8	32	1.71	1.71	1.71	1.71	1.71	1.71	1.71	1.71	3.44
4	3.2	8	32	2.20	7.07	16.8	24.1	38.6	43.4	50.7	53.1	4.42
5	0.8	2	68	12.5	10.4	11.0	17.1	27.8	42.9	48.3	55.8	4.25
6	3.2	2	68	85.0	90.0	90.1	87.8	90.4	96.7	96.7	96.8	379
7	0.8	8	68	0.98	2.93	8.53	31.6	51.6	93.5	94.7	95.1	8.10
8	3.2	8	68	85.0	85.1	85.2	85.4	88.0	90.0	90.1	90.2	379
9	0,0	5	50	3.93	4.16	4.51	5.21	10.8	11.5	21.7	22.3	1.32
10	4.0	5	50	72.5	77.5	85.0	85.1	87.7	89.2	90.2	98.9	258
11	2.0	0	50	0.87	2.61	7.92	8.60	9.28	12.4	13.0	16.0	0.88
12	2.0	10	50	7.38	7.61	12.9	35.6	45.8	55.8	60.9	68.2	6.41
13	2.0	5	20	2.14	2.14	2.14	2.14	2.14	2.14	2.14	2.14	4.32
14	2.0	5	80	80.0	91.2	91.5	91.9	91.8	92.0	92.1	93.1	322
15-20	2.0	5	50	2.44 ±0.00	7.28 ±0.46	14.2 ±1.25	23.5 ±0.50	33.5 ±1.30	47.7 ±1.85	51.2 ±1.36	58.3 ±2.43	4.89 ±0.28

Linear regression analysis was used to calculate the rate constants (k). High correlations ($R^2 \geq 0.91$, except Exp.1 with $R^2=0.57$) showed the consistency of experimental data with the model (Eq. 6). Previous researchers [40] also confirmed that decomposition of hydrogen peroxide follows first-order reaction kinetics.

Analysis of variance (ANOVA) was applied to test the significance of regression terms (i.e. parameters) using P-values (Table 5). All the regression models were statistically significant even at a confidence level of 99.9% ($\alpha=0.001$). Linear (main) effects of pH and temperature on decomposition of peroxide at different periods and decomposition kinetics were statistically significant at the same confidence level of 99.9% ($\alpha=0.001$) (Table 5). A positive mode of effect (Table 4) indicates that increasing the pH and temperature facilitates the rate and extent of decomposition of peroxide. The effect of copper on the extent of decomposition was not statistically significant during the initial periods of 5-30 min. at 95% confidence level ($\alpha=0.05$) (Table 5). However, over extended periods (≥60 min.), its effect became significant (Table 4). No significant effect of copper (i.e. $P<\alpha=0.05$) was detected on the decomposition kinetics (Table 5). The quadratic effects of pH (A^2) and temperature (C^2), and their interaction effect (AC) on the decomposition rate and extent of H_2O_2 were found to be statistically significant at 95% confidence level ($\alpha=0.05$) between the periods of 5 and 90 min. (except for 90 min. which is significant at 90% confidence level ($\alpha=0.1$)) (Table 5).

The surface plots (Figs. 1 and 2) illustrate simultaneous effects of parameters on each response (i.e. decomposition extent (%) at 180 min. and rate constant (k, min^{-1})). High temperature and high pH appeared to aggravate the rate and extent decomposition of hydrogen peroxide (Figs. 1-2). Simultaneously, elevating the levels of pH, temperature and copper was found to produce a synergistic adverse effect on the stability of hydrogen peroxide. It is also evident from the surface plots that decomposition of hydrogen peroxide (Fig. 1) also increases with increasing the concentration of copper though its effect on the decomposition rate is relatively limited (Fig. 2). Mlasi et al. [40] investigated the effect of copper on the decomposition of hydrogen peroxide under the conditions of 1 M H_2SO_4 at 67°C. The researchers found that increasing the addition of copper sulphate by 4-fold led to a 1.74-fold increase in the rate of decomposition of hydrogen peroxide.

Table 4 Regression coefficients of the mathematical models

Terms	Regression Coefficients								
	Decomposition of H_2O_2 (%)								Rate constant
	5 min	15 min	30 min	60 min	90 min	120 min	150 min	180 min	k (min^{-1})
Constant	2.61	7.50	14.46	23.69	33.65	46.56	49.31	53.35	5.11
A-pH	20.16	21.49	22.64	21.18	20.00	17.08	16.18	17.33	86.33
B-Cu(II)	-0.23	-0.13	0.95	5.25	8.17	10.84	11.43	11.09	1.38
C-Temp.	22.26	23.65	23.44	24.58	26.12	30.38	30.19	30.20	94.85
AB	1.12	0.61	1.21	-0.31	0.35	-	-	-	-0.37
AC	19.13	19.17	17.20	11.77	6.76	-	-	-	93.18
BC	-1.11	-1.84	-2.43	-0.28	-0.93	-	-	-	-0.24
A^2	11.56	10.42	9.18	6.28	4.91	-	-	-	42.65
B^2	-0.48	-2.21	-2.97	-1.88	-2.77	-	-	-	-1.89
C^2	12.58	12.49	9.90	6.94	4.11	-	-	-	54.50
R^2 of the model	*0.99*	*0.99*	*0.98*	*0.97*	*0.97*	*0.90*	*0.91*	*0.90*	*1.00*

Table 5 Statistical significance of the effect of parameters and interactions on decomposition rate and extent of hydrogen peroxide (%)

Source	P - values								
	Decomposition of H_2O_2 (%)								Rate constant
	5 min	15 min	30 min	60 min	90 min	120 min	150 min	180 min	k (min^{-1})
Model	< 0.0001	< 0.0001	< 0.0001	< 0.0001	< 0.0001	< 0.0001	< 0.0001	< 0.0001	< 0.0001
A-pH	< 0.0001	< 0.0001	< 0.0001	< 0.0001	< 0.0001	< 0.0001	< 0.0001	< 0.0001	< 0.0001
B-Cu(II)	0.8343	0.9255	0.5609	0.0155	0.0025	0.0024	0.0012	0.0026	0.6405
C-Temp.	< 0.0001	< 0.0001	< 0.0001	< 0.0001	< 0.0001	< 0.0001	< 0.0001	< 0.0001	< 0.0001
AB	0.4465	0.7392	0.5690	0.8977	0.8990	-	-	-	0.9241
AC	< 0.0001	< 0.0001	< 0.0001	0.0005	0.0295	-	-	-	< 0.0001
BC	0.4526	0.3274	0.2649	0.9063	0.7334	-	-	-	0.9505
A^2	< 0.0001	< 0.0001	0.0001	0.0050	0.0330	-	-	-	< 0.0001
B^2	0.6592	0.1274	0.0811	0.3102	0.1938	-	-	-	0.5150
C^2	< 0.0001	< 0.0001	< 0.0001	0.0027	0.0652	-	-	-	< 0.0001
R^2 of the model	*0.99*	*0.99*	*0.98*	*0.97*	*0.97*	*0.90*	*0.91*	*0.90*	*1.00*

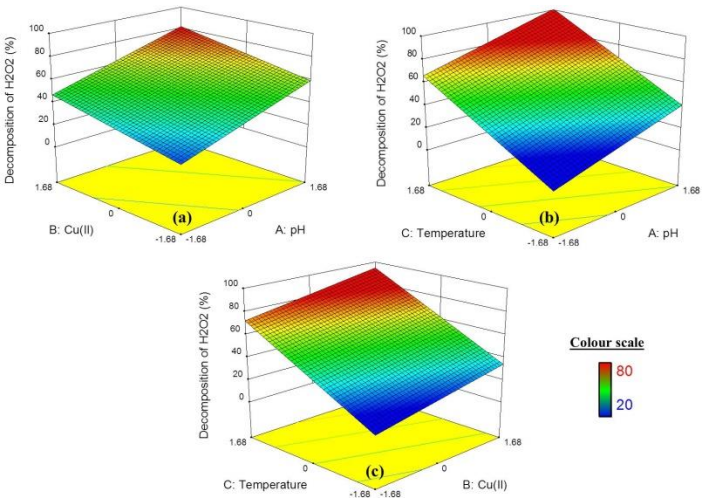

Figure 1 Response surface plots demonstrating the simultaneous effects of parameters on the extent of decomposition of H_2O_2 (at 180 min.) (the third parameter was held at centre level), (a) pH and concentration of Cu(II) (*AB*), (b) pH and Temperature (AC); (c) Concentration of Cu(II) and Temperature (*BC*) ($[H_2O_2]_0$: 0.5 M)

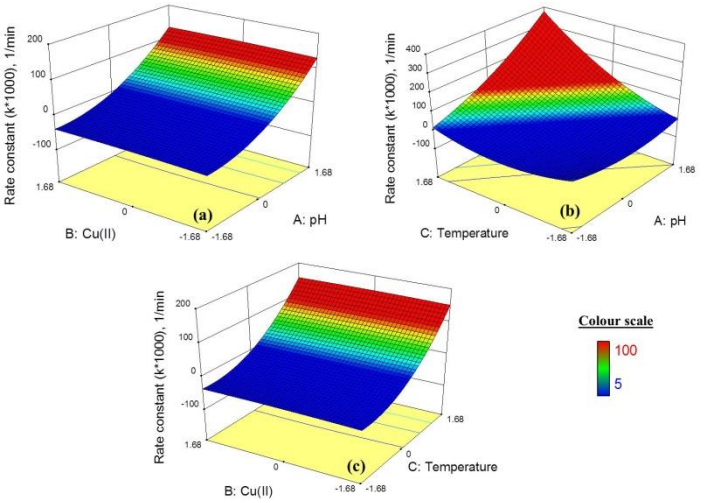

Figure 2 Response surface plots demonstrating the simultaneous effects of parameters on the decomposition kinetics of H_2O_2 ($k.10^3$ min^{-1}) (the third parameter was held at centre level), (a) pH and concentration of Cu(II) (*AB*), (b) pH and Temperature (AC); (c) Concentration of Cu(II) and Temperature (*BC*) ($[H_2O_2]_0$: 0.5 M)

Considering the prime importance of temperature for the stability of hydrogen peroxide (Table 5), the activation energies (E_a) were calculated using Arrhenius equation based on the data obtained in the absence and presence of PBS (2.5-20 $ml.l^{-1}$) (Fig. 3). The mean value for the activation energy was 60.7±2.5 $kJ.mol^{-1}$ indicating a chemically controlled process (i.e. E_a>25 $kJ.mol^{-1}$) [41].

Decomposition of peroxide under neutral and alkaline conditions (pH 7.3-11.8) was also tested separately (Fig. 4). Elevating the pH from neutral to alkaline led to a decrease in the stability of peroxide particularly at >pH 9.8. While only ≤7.4% of peroxide decomposed at ≤pH 9.8 over 180 min., it increased to 39% at pH 11.8. Under alkaline conditions, hydrogen peroxide decomposes according to Eq. 6 [3].

$$H_2O_{2\,(aq)} \rightarrow H^+ + HO_2^- \qquad (6)$$

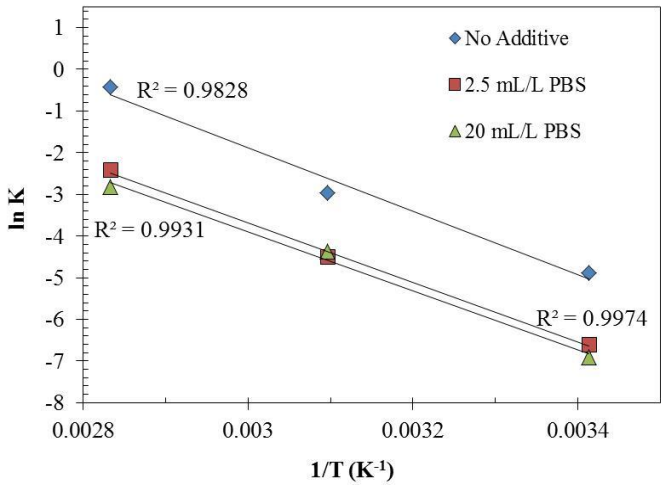

Figure 3 Arrhenius plots (ln K vs. K^{-1}) for decomposition of hydrogen peroxide in the absence and presence of PBS (2.5-20 $ml.l^{-1}$) (pH 4, 5 $g.l^{-1}$ Cu(II), $[H_2O_2]_0$: 0.5 M)

Consistent with the current findings (Fig. 4, Table 4-5), Yazıcı and Deveci [27] reported that increasing the concentration of copper (10-40 $mg.l^{-1}$ Cu), solids ratio (0-4 w/v), temperature (20-50°C) and pH (9.5-12) resulted in the increased consumption of hydrogen peroxide. Lee et al. [42] compared the effects of NaOH and Na_2CO_3 for pH adjustment (pH 10.0-10.6) on the stability of hydrogen peroxide over 2 h. They found that hydrogen peroxide was relatively less stable in carbonate media since carbonate (or bicarbonate) anion promotes decomposition of hydrogen peroxide. They concluded that NaOH is a more suitable pH-modulating reagent than Na_2CO_3.

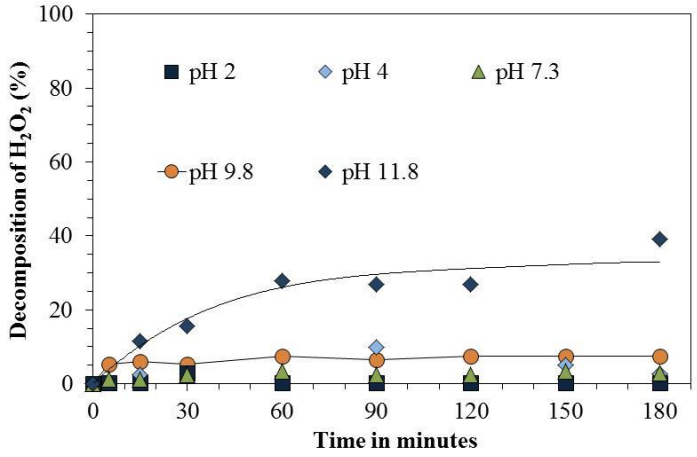

Figure 4 Effect of acid, neutral and alkaline pHs on the decomposition of H_2O_2 (%) ($[H_2O_2]_0$: 0.5 M, no Cu(II), 20°C)

Effect of solids

The effect of solids on the stability of hydrogen peroxide is of practical importance since solids are present in many processes (e.g. leaching of ores/metals and or treatment of pulps/effluents) where peroxide is used as an effective oxidant [6,7,16,43]. The effect of solids (1-20% w/v) on the stability of hydrogen peroxide was investigated under different pH and temperature conditions. At 20°C, the effect of solids on the decomposition of hydrogen peroxide was limited to only ≤5% at pH 2-4 over 180 min. (figure not shown). These results suggested that hydrogen peroxide is quite stable at low temperatures (i.e. 20°C) and acidic pHs (<pH 4) even in the presence of solids by up to 20% w/v. However, at high temperatures (e.g. at 80°C) a two-fold increase

in the loss of hydrogen peroxide was observed in the presence of solids (10 w/v) i.e. from 21% (no solids) to 42% (10% w/v solids) over 180 min. (Fig. 5). Yazıcı and Deveci [27] studied the effect of solids (1-4% w/v quartz) on the decomposition of hydrogen peroxide at an alkaline pH of 10.5-11. The researchers found that an increase in the concentration of solids from none to 4% w/v resulted in a 27% loss of hydrogen peroxide at 180 min.

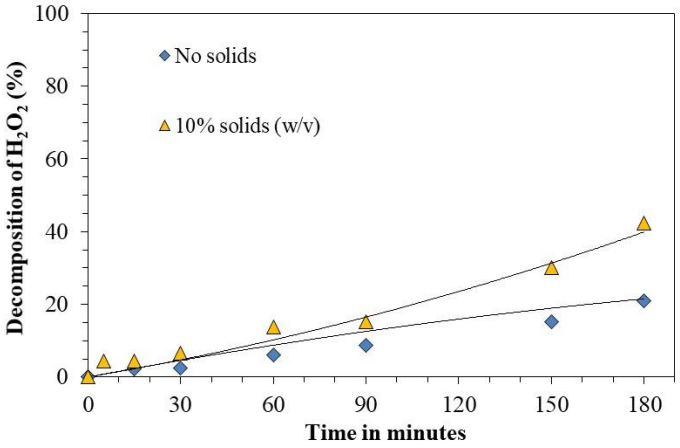

Figure 5 Effect of solids on the decomposition of H_2O_2 (%) at pH 2 and 80°C ($[H_2O_2]_0$: 0.5 M, no Cu)

Effect of addition of the polycarboxylate based solution (PBS)

The influence of a polycarboxylate based solution (PBS) as the additive on the stability of hydrogen peroxide was tested in the absence/presence of copper (5 $g.l^{-1}$) under different experimental conditions of pH (2-4) and temperature (20-80°C) (Figs. 6-8). The addition of PBS significantly prolonged the rate and extent of decomposition of hydrogen peroxide in the presence of copper (Figs. 6-7). This improvement was more apparent at low-temperature conditions (i.e. 20°C) (Fig. 6b) than at high temperatures of 50-80°C (Fig. 6a,c and Fig. 7a,b). To exemplify, in the presence of copper (5 $g.l^{-1}$) at pH 4 and 20°C, the addition of PBS at the dosage of 2.5 $ml.l^{-1}$ led to a 56% decrease (from 73% to 17%) in consumption of hydrogen peroxide over 180 min. (Fig. 6b) while only 9% (from 99% to 90%) (Fig. 6c) and 0.4% (from 99.4% to 99.0%) (Fig. 7b) reduction in the decomposition of hydrogen peroxide was obtained at 50°C and 80°C, respectively, over the same period.

In the presence of 5 $g.l^{-1}$ Cu at pH 2 and 50°C, increasing the dosage of PBS (> 2.5 $ml.l^{-1}$) was sufficient for stabilisation of hydrogen peroxide (Fig. 6a) while under highly aggressive conditions (i.e. pH 4 and 80°C) even at 20 $ml.l^{-1}$ dosage most of the peroxide (i.e. 97%) was consumed in 60 min. (Fig. 6b). At 80°C an extensive decomposition of hydrogen peroxide (by ≥88% at 60 min.) occurred even at the highest concentration of PBS tested (20 $ml.l^{-1}$) (Fig. 7). It can be deduced from these results (Figs. 6-7) that under severe conditions i.e. at high levels of pH, temperature and copper, stabilising the effect of PBS on hydrogen peroxide becomes limited.

The contribution of PBS to the stability of hydrogen peroxide (Figs. 6-7) could be linked with the complexing ability of polycarboxylates with copper reducing the reactivity of copper ions [44,45]. It is pertinent to note that the addition of PBS was observed to lead to a change in the colour of the solution from blue to green, which is indicative of the formation of copper-polycarboxylate complexes. In a previous work by Bas et al. [46], the addition of PBS in cyanide leaching of a copper-rich gold ore resulted in reduced consumption of free cyanide by 39%. The authors attributed this effect to the complexation of copper with polycarboxylates, which reduces the formation of copper-cyanide complexes.

The decomposition of hydrogen peroxide was also monitored in the absence of copper at pH 2 (50-80°C) and pH 4 (20-50°C) with/without the addition of PBS (2.5-20 $ml.l^{-1}$). Hydrogen peroxide decompositions (%) was recorded to be 18.1% (pH 2, 50°C), 21.2% (pH 2, 80°C), 5.0% (pH 4, 20°C) and 16.4% (pH 4, 50°C) over the period of 180 min. in the absence of PBS (figure not shown). The addition of PBS (2.5-20 $ml.l^{-1}$) had no effect on the stability of peroxide under the conditions tested. It can be inferred from these findings that the contribution of PBS to the stability of peroxide is essentially linked with the impediment of the catalytic effect of copper.

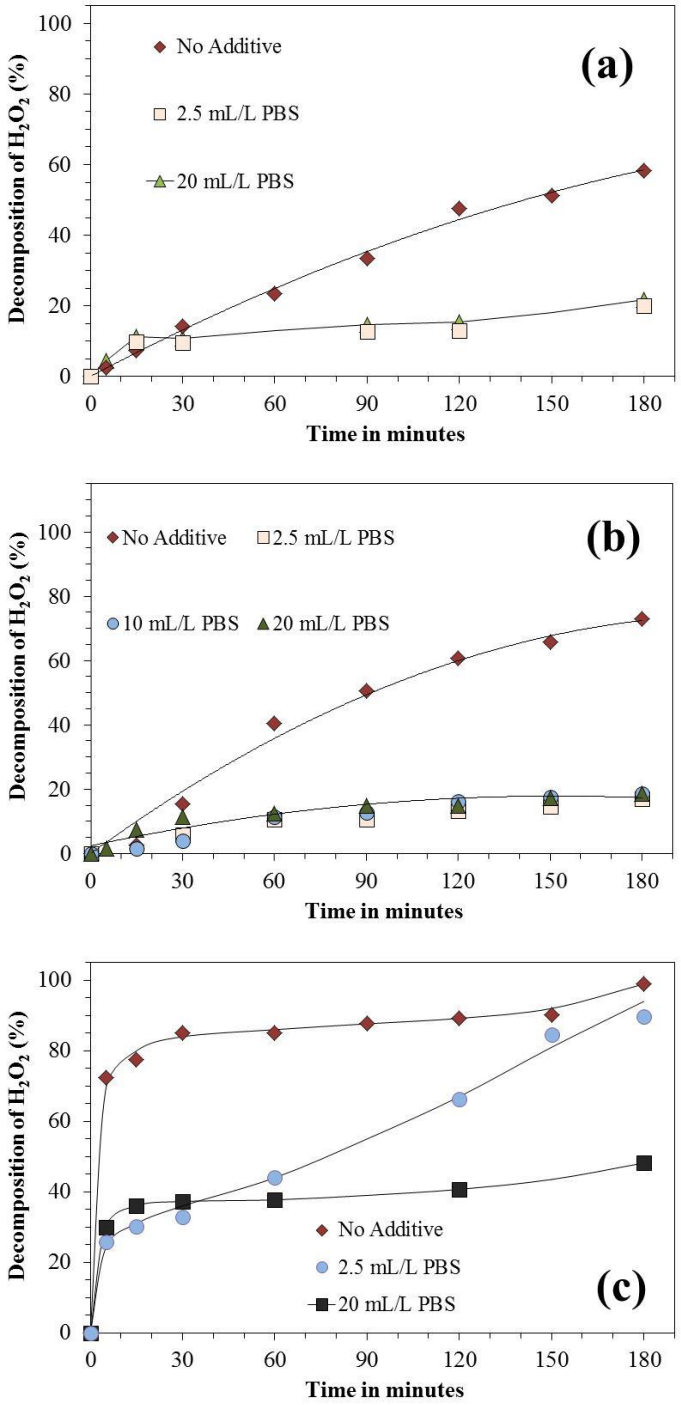

Figure 6 Effect of addition of polycarboxylate based solution (PBS) on the decomposition of H_2O_2 (%) in the presence of 5 $g.l^{-1}$ Cu(II) at 20-50°C (a) pH 2, 50°C, (b) pH 4, 20°C, (c) pH 4, 50°C ($[H_2O_2]_0$: 0.5 M)

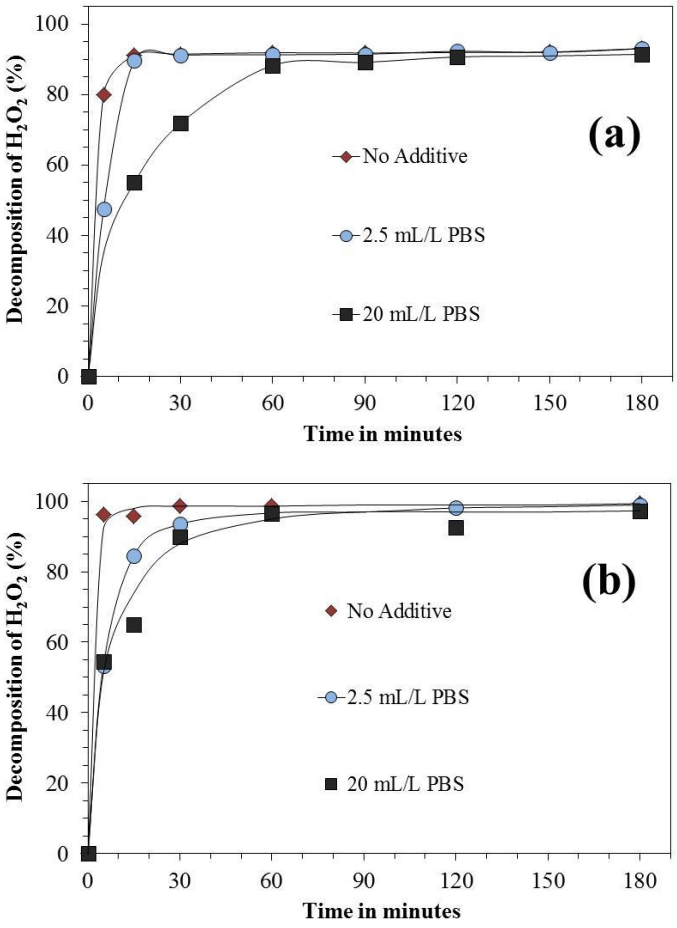

Figure 7 Effect of addition of polycarboxylate based solution (PBS) on the decomposition of H_2O_2 (%) in the presence of 5 g.l^{-1} Cu(II) at 80°C (a) pH 2, (b) pH 4 ($[H_2O_2]_0$: 0.5 M)

Demonstration of PBS addition in hydrogen peroxide leaching of e-waste

Hydrogen peroxide can be suitably used as an oxidant for leaching of base (mainly Cu) and precious metals (Au, Ag and Pd) in sulphate/chloride media from waste electrical and electronic equipments (WEEE or e-waste) [43,47-49] in which copper content can reach up to 20% [10,50]. During leaching of e-waste, copper, as well as other metals, would dissolve and facilitate catalytic decomposition of hydrogen peroxide, which may result in low metal recoveries and high reagent consumption. Therefore, stabilisation of hydrogen peroxide is of practical importance in hydrogen peroxide leaching of e-waste.

To demonstrate the practical application of PBS for a real process, leaching tests in H_2SO_4+H_2O_2 solutions were performed using the waste of printed circuit boards (WPCBs) in the absence and presence of PBS (Fig. 8). Effect of PBS (1.3-6.7 ml.l^{-1}) on the extraction of copper from WPCBs was tested under the conditions of 1 M H_2SO_4, 1 M H_2O_2, %1 w/v solids at 80°C. In the absence of PBS, copper leaching was limited to ≈81% over the period of 0.25-0.5 h (Fig. 8). The addition of PBS led to a significant improvement in extraction of copper by up to 19% i.e. from ≈81% (no PBS) to complete extraction (6.7 ml.l^{-1} PBS) over 0.25-0.5 h. The enhancing effect of PBS on copper leaching (Fig. 8) can be essentially ascribed to the stabilisation of hydrogen peroxide through complexation of PBS with metals, copper in particular (Eqs. 2-3). Final redox potentials also indicated the contribution of PBS to stabilisation of hydrogen peroxide in that higher redox potentials were recorded in the presence of PBS i.e. 277 mV (no PBS) *vs.* 297 mV (1.3 ml.l^{-1} PBS) *vs.* 316 mV (6.7 ml.l^{-1} PBS) (Fig. 9) apparently due to the relatively high residual concentration of hydrogen peroxide in the presence of PBS. These results (Fig. 9) justify that PBS can be suitably employed to enhance leaching of metals in hydrogen peroxide assisted lixiviant systems.

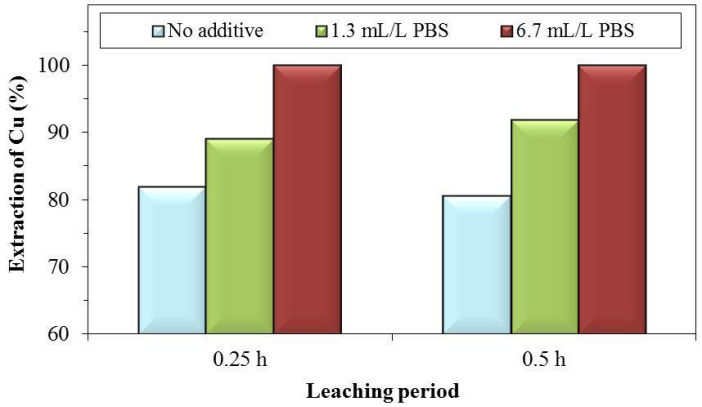

Figure 8 Effect of addition of PBS on extraction of copper from WPCBs in H_2SO_4+H_2O_2 solutions ($[H_2SO_4]$: 1 M, $[H_2O_2]_0$: 1, 80°C, %1 w/v solids)

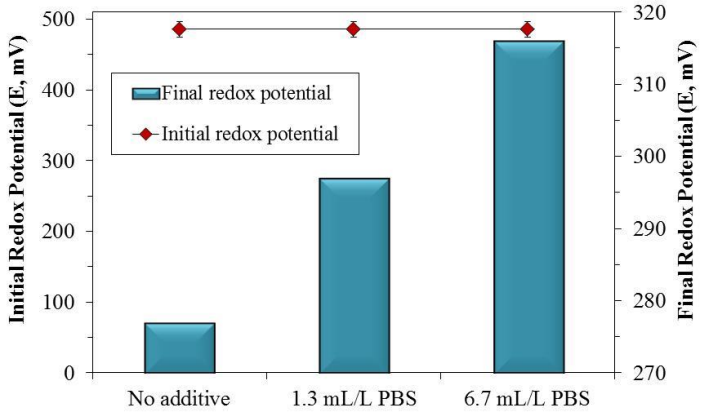

Figure 9 Initial and final redox potentials ($E_{Ag/AgCl}$, mV) in leaching of copper from WPCBs by H_2SO_4+H_2O_2 solutions in the absence and presence of PBS (1.3-6.7 ml.l^{-1})

CONCLUSION

Due to superior oxidising potential and its consideration as green chemical, hydrogen peroxide is extensively utilised in various industries. However, the main detraction to hydrogen peroxide is its catalytic decomposition leading to prohibitively high reagent consumption. The effect of various parameters i.e. pH (0-4), the concentration of Cu(II) (0-10 g.l^{-1}) and temperature (20-80°C) on the rate and extent of decomposition of hydrogen peroxide was studied using design of experiments at five levels. The tests were extended to cover the effect of neutral and alkaline pH of 7.3-11.8) and solids (1-20% w/v). A commercial polycarboxylate based reagent (PBS, 2.5-20 ml.l^{-1}) was tested as the additive to improve stability of hydrogen peroxide in the absence/presence of copper. The results have demonstrated that decomposition of hydrogen peroxide aggravates with increasing temperature, pH and copper in descending order of significance. The calculated activation energy (E_a) of 60.7±2.5 kJ.mol^{-1} for decomposition of H_2O_2 indicates a chemically controlled reaction. The presence of solids was also found to adversely affect the stability of hydrogen peroxide, particularly at high temperature of 80°C. The addition of PBS was shown to significantly mitigate the catalytic decomposition of hydrogen peroxide in the presence of copper i.e. 58.3% decomposition of peroxide (no additive) compared with to 20.1% (at 2.5 ml.l^{-1} additive) in the presence of 5 g.l^{-1} Cu(II) at pH 2 and 50°C over 3 h. However, stabilising effect of PBS even at high dosages tested (20 ml.l^{-1}) was very limited at high pH and/or temperature. Contribution of PBS to the stability of H_2O_2 was observed only in the presence of copper. This was attributed to the

complexing ability of PBS with copper. The beneficial effect of PBS (1.3-6.7 $ml.l^{-1}$) on H_2O_2 leaching of copper from a waste of printed circuit boards (WPCBs) was also demonstrated i.e. up to 19% improvement in leaching of copper in the presence of PBS. These findings suggest that PBS can be suitably employed to mitigate catalytic decomposition of H_2O_2 in the presence of copper in applications where it is utilised.

REFERENCES

[1] D. R. Lide: *CRC Handbook of chemistry and physics*, CRC Press, Boca Raton, FL, 2005
[2] [19.08.2016], http://h2o2.evonik.com/product/h2o2/en/about-hydrogen-peroxide/basic-information/stability-and-decomposition
[3] C. W. Jones: *Applications of hydrogen peroxide and derivatives*, Royal Society of Chemistry, 1999
[4] J. Marsden, I. House: *The chemistry of gold extraction*, Society for Mining, Metallurgy, and Exploration, USA, 2006
[5] W. G. I. Davenport, M. King, M.Schlesinger, A.K. Biswas: *Extractive metallurgy of copper*, Pergamon, UK, 2002
[6] D. Dreisinger: Hydrometallurgy, 83(1–4), 10-20. https://doi.org/10.1016/j.hydromet.2006.03.032
[7] Tuncuk, A., Stazi, V., Akcil, A., Yazici, E.Y., & Deveci, H. (2012) Aqueous Metal Recovery Techniques from E-scrap: Hydrometallurgy in Recycling. Min. Eng., 25(1), 2006, 28-37. https://doi.org/10.1016/j.mineng.2011.09.019
[8] M. D. Turan, H. S. Altundoğan: Metallurgical and Materials Transactions B, 44(4), 2013, 809-819. https://doi.org/10.1007/s11663-013-9858-0
[9] H. R. Watling, (2013): Hydrometallurgy, 140, 2013, 163-180. https://doi.org/10.1016/j.hydromet.2013.09.013
[10] E. Y. Yazici: Recovery of Metals from E-wastes by Physical and Hydrometallurgical Processes. Karadeniz Technical University, PhD Thesis, 2012
[11] V. I. Lakshmanan, R. Roy, V. Ramachandran: *Innovative process development in metallurgical industry*, Springer, 2016
[12] C. K. Gupta, T. K. Mukherjee: *Hydrometallurgy in extraction processes*, CRC Press, Boston, 1990
[13] F. Habashi: *Textbook of hydrometallurgy*, Metallurgie Extractive Quebec, 1999
[14] M. M. Botz, T. I. Mudder, A. U. Akcil: Cyanide treatment: Physical, chemical and biological processes. In: *Developments in Mineral Processing*, edited by D. A. Mike, B. A. Wills, Elsevier, 2005, p. 672-702.
[15] N. Kuyucak, A. Akcil: Min. Eng., 50–51, 2013, 13-29. https://doi.org/10.1016/j.mineng.2013.05.027
[16] T. I.Mudder, M. M. Botz: *The chemistry and treatment of cyanidation wastes*, Mining Journal Books Ltd., London, 2001
[17] E. Y.Yazıcı, H. Deveci, I. Alp, T. Uslu, O. Celep: Factors Affecting Decomposition of Cyanide by Hydrogen Peroxide. In.: *XXIII. Int. Mineral Processing Congress (IMPC)*, Istanbul, Turkey, 2006, p. 2439-2444
[18] [19.09.2016], http://h2o2.evonik.com/product/h2o2/en/application-areas/pages/default.aspx
[19] J. Sharma, I. M. Mishra, V. Kumar: Journal of Environmental Management, 156, 2015, 266-275. https://doi.org/10.1016/j.jenvman.2015.03.048
[20] W. P. Kwan, B. M. Voelker: Environ. Sci. Technol., 36(7), 2002, 1467-1476. https://doi.org/10.1021/es011109p
[21] F. J. Miner, R. G. Hagan: Ind. Eng. Chem. Process Des. Dev., 11(4), 1972, 547-549. https://doi.org/10.1021/i260044a017
[22] B. G. Petri, R. J. Watts, A. L. Teel, S. G. Huling, R. A. Brown: Fundamentals of ISCO Using Hydrogen Peroxide, In: *In Situ Chemical Oxidation for Groundwater Remediation*, edited by L. R. Siegrist, M. Crimi, J. T. Simpkin, Springer, New York, 2011, p. 33-88.
[23] W. C. Schumb: .Industrial & Engineering Chemistry, 41(5), 1949, 992-1003. https://doi.org/10.1021/ie50473a026
[24] V. S. Shivankar, N. V. Thakkar: J. Sci. Ind.Res., 64, 2005, 496-503.
[25] A. Hiroki, J. A. LaVerne: The Journal of Physical Chemistry B, 109(8), 2005, 3364-3370. https://doi.org/10.1021/jp046405d
[26] R. M. Khalil: J. of King Abdulaziz University, 2, 1990, 91-100.
[27] E. Y. Yazıcı, H. Deveci: Factors Affecting Decomposition of Hydrogen Peroxide, In.: *XII. International Mineral Processing Symposium (IMPS)*, Kapadokya, Turkey, 2010, p. 609-616
[28] Q. G. Hopkins, J. N. Browning: Stabilization of high purity hydrogen peroxide, FMC Corporation, 4,534,945, US Patent, 1985
[29] K. Itani, Y. Miyashiro: Method for stabilizing acidic aqueous hydrogen peroxide solution containing copper, 5,211,927, US Patent, 1992
[30] K. Kushibe: Method of stabilizing acid aqueous solutions of hydrogen peroxide, 3,933,982, US Patent, 1976
[31] D. C. Winkley: Stabilization of iron-containing acidic hydrogen peroxide solutions, FMC Corporation, 4,059,678, US Patent, 1977
[32] V. Mahajan, M. Misra, K. Zhong, M. C. Fuerstenau: Min. Eng., 20(7), 2007, 670-674. https://doi.org/10.1016/j.mineng.2006.12.016
[33] A. D.Bas, E. Y. Yazici, H. Deveci: Hydrometallurgy, 121–124, 2012, 22-27. https://doi.org/10.1016/j.hydromet.2012.04.011
[34] Á. Ruiz-Sánchez, G. T. Lapidus: Hydrometallurgy, 169, 2017, 192-200. https://doi.org/10.1016/j.hydromet.2017.01.014
[35] Iksa, Technical Brochure for Polycar 100, 201.
[36] G. H. Jeffery, J. Bassett, J. Mendham, R.C. Denney: *Vogel's textbook of quantitative chemical analysis*, John Wiley & Sons Inc, 1989
[37] P. G. Mathews: *Design of experiments with MINITAB*, ASQ Quality Press, USA, 2005
[38] D. C. Montgomery: *Design and analysis of experiments*, Wiley. 2001
[39] Design-Expert, DOE Software, Stat-Ease Inc., Minneapolis, USA, 8.0.7.1, USA, 2010
[40] B. Mlasi, D. Glasser, D. Hildebrandt: Ind. Eng.Chem. Res., 54(21), 2015, 5589-5597. https://doi.org/10.1021/acs.iecr.5b00642
[41] S. Robertson, M. Jeffrey, H. Zhang, E. Ho: Metall. Mater. Trans. B, 36(3), 2005, 313-325. https://doi.org/10.1007/s11663-005-0061-9
[42] H. H. B. Lee, A.-H. Park, C. Oloman: TAPPI JOURNAL, 83(8). 2000, 1-9.
[43] H. Deveci, E. Y. Yazıcı, U. Aydın, R. Yazıcı, A. U. Akçil: Extraction of copper from scrap TV boards by sulphuric acid leaching under oxidising conditions, In.: *Going Green-Care Innovation*, Vienna, Austria, 2010, paper no: 045
[44] J. A.McCleverty, T. J. Meyer: *Comprehensive coordination chemistry II: from biology to nanotechnology*, Elsevier Science, 2003
[45] S. Paoletti, F. Delben, V. Crescenzi: The Journal of Physical Chemistry, 80(23), 1976, 2564-2568. https://doi.org/10.1021/j100564a008
[46] A. D Bas, E. Y. Yazici, H. Deveci: Treatment of a copper-rich gold ore by ammonia assisted cyanide leaching, In.: *XXVI. International Mineral Processing Congress (IMPC)*, New Delhi, 2012, p. 356-365
[47] I. Birloaga, I. De Michelis, F. Ferella, M. Buzatu, F. Vegliò: Waste Manage., 33(4), 2013, 935-941. https://doi.org/10.1016/j.wasman.2013.01.003
[48] Ž. Kamberović, M. Korać, S. Vračar, M. Ranitović: Preliminary Process Analysis and Development of Hydrometallurgical Process for the Recovery of Copper from Waste Printed Circuit Boards, In.: *Going Green-Care Innovation Conference*, Vienna, Austria, 2010, Paper-no:IS05c
[49] Z. Wang, S. Guo, C. Ye: Procedia Environ. Sci., 31, 2016, 917-924. https://doi.org/10.1016/j.proenv.2016.02.110
[50] C. Hagelüken: Improving Metal Returns and Eco-efficiency in Electronics Recycling - A Holistic Approach for Interface Optimisation Between Pre-processing and Integrated Metals Smelting and Refining, In.: *Proceedings of International Symposium on Electronics and the Enviroment (ISEEE)*, Scottsdale, AZ, USA, 2006, p. 218-223

OPEN ACCESS

ACTA METALLURGICA SLOVACA

2020, VOL. 26, NO. 1, 24-26

RESEARCH PAPER

AUSTENITIC STAINLESS STEELS MANUFACTURING BY LASER POWDER BED FUSION TECHNIQUE

Andrea Di Schino[1)], Paolo Fogarait[2], Domenico Corapi[2], Orlando Di Pietro[1], Chiara Zitelli[1]*

[1)]*Università degli Studi di Perugia, Dipartimento di Ingegneria, Perugia, Italy*

[2)] *Seamthesis Srl, Piacenza, Italy*

**Corresponding author: andrea.dischino@unipg.it, Università degli Studi di Perugia, Dipartimento di Ingegneria, Via G. Duranti 93, 06125 Perugia, Italy*

Received: 10.11.2019
Accepted: 03.02.2020

ABSTRACT

In this paper we report about the possibility to process stainless steels by laser powder bed fusion (L-PBF) systems. Austenitic stainless steels are analysed showing the possibility to successfully process them, targeting different applications. In particular, it is shown that stainless steels can be successfully processed and their mechanical behaviour allow them to be put in service. Porosities inside manufactured components are extremely low and comparable to conventionally processed materials. Mechanical performances are even higher than standard requirements. Micro surface roughness typical of the as-built material can act as crack initiator, reducing the strength in both quasi-static and dynamic conditions.

Keywords: Stainless steels; laser powder bed fusion; additive manufacturing

INTRODUCTION

Stainless steels are nowadays applied in quite different applications due to their peculiar properties in terms of strength/ductility requirements coupled with corrosion resistance high targets. In particular, they are adopted in automotive [1-10], construction and building [11-12], energy [13-15], aeronautical [17], medical [18], food [19-24] and 3D printing [25-29] applications. Additive manufacturing (AM) is an emerging technology able to manufacture near-net-shape components characterized by complex geometries. AM is particularly suited for small production amounts, in particular in those cases requiring part-customization and functional integration: this is why it first emerged as a rapid prototyping technology. The adoption of AM technologies resulted in new production paradigm [30-33] since the designer is now able to project a component, or customize the geometry of an already-existing one, taking into account the final service conditions. At the meantime, AM allows to simplify components assembly by merging different parts in one single monolith.
The possibility to manufacture stainless steel components in laser powder bed fusion (L-PBF) systems, accomplished with a deeper methodology understanding, will result in a larger adoption of the technology itself. Nowadays L-PBF has been already applied to manufacture stainless steel components, but a basic lack in standardisation and correct metrology definition is limiting the possibility to adopt such technology for standard production: for this reason international committees are joining together to accelerate the process. The challenge is to consistently define the ideal processing routes and requirements, standard mechanical requirements, suitable heat treatments, dynamic performances, post-processing and qualification needs. This paper will focus on the state of the art of stainless steel alloys application in L-PBF systems: starting from the working conditions a list of stainless steel grades already tested on L-PBF systems is reported with their main properties.

Austenitic stainless steel processing in L-PBF system

Stainless steels are worldwide adopted following their peculiar properties combination (both at room and high temperature) thanks to their chemical composition and microstructural details. In L-PBF, the correct steel chemical composition is guaranteed by a wise manipulation and correct storing of adopted metal powders, mainly to avoid the oxygen presence; on the contrary, microstructural features (e.g. grain size, precipitation state) are achieved by 3D printing parameters. In particular, final product microstructure depends on the local heat flow direction, grains competitive growth and laser scanning strategy. Typical cooling rates are in the range 105-106 K/s [34] following the gas atmosphere heat exchange with the not yet fused powder and the underneath material already consolidated: the so obtained solidified microstructure is fine and far from that provided by thermodynamic equilibrium. Moreover, laser scanning strategy impacts on the material texture: for example, in the case of no rotation between subsequent layers during scanning, the as-built material will be characterized by a strong <0 0 1> texture as a preferential grain growth direction this will lead to a strongly orthotropic steel behaviour. On the other side, if powder bed is scanned in small islands, also non-consecutive, and rotation of laser between different layers is adopted, an almost untextured microstructure is achieved. Elongated grain structure, along z-direction (according to Figure 1), is due to both heat extraction from the bottom side of the melt pool (i.e. building substrate) and epitaxial grain growth, like fusion welding. In L-PBF the existing base-metal grains (i.e. the grains existing in the last melted layer) act as substrate for nucleation. Moreover, if subsequent layers are melted, this will cause reheating of the already consolidated material, determining solid state phase transformations.

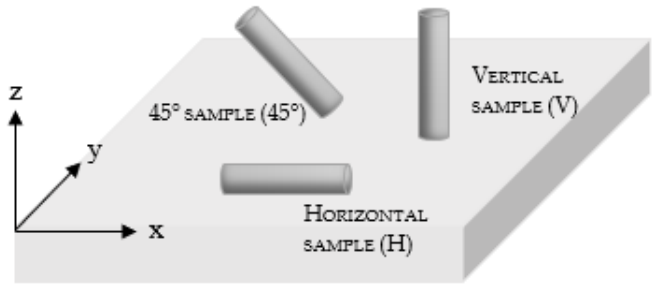

Fig.1 Schematics of commonly projected building directions for tensile specimens.

The particular microstructures coming from the above reported physical phenomena determine different mechanical behaviour as a function of the tested direction or on the service loading condition. This is the reason why the best rule is to produce tensile specimens with their main axis oriented along different directions, as schematised in Figure 1: vertical specimens (V) are representative of commonly identified longitudinal direction, while horizontal specimens (H) of transversal direction. The above reported peculiar metallurgical behaviour of materials produced via AM, led Murr et al. [35] to affirm that such methodology could extend traditional materials science and engineering, as far as allowing planning application-specific microstructural architecture in as-built components.

RESULTS

Just a few austenitic stainless steel grades are nowadays manufactured by L-PBF process: AISI 304, AISI 304L and AISI 316L are the most common ones, the latter being the only one of them commercialized by systems manufacturers.
In Table 1 tensile testing results are reported and compared to standard minimum requirements, showing that:

- room temperature properties result higher than the minimum requirements usually applied for the selected stainless steel grades processed with conventional technologies, apart from fracture elongation;
- fracture elongation is the most negatively affected parameter, for samples tested in the as built condition;

Table 1 Tensile strength of austenitic stainless steel grades obtained from L-PBF, compared to standard reference values (BD= Building Direction; YS= Yield Strength; UTS= Ultimate Tensile Strength; El.= Elongation; SD= Self-developed; NR= Non reported; RT= Room Temperature; HT= Heat Treated; H= Horizontal; V= Vertical).

Grade	Equipment	Relative density [%]	Cond.	BD	Test cond.	YS [MPa]	UTS [MPa]
304	SD	NR	As built	H	RT	530	700
				45°		370	540
				V		450	550
304L	3D Systems ProX-300	99,99	As built	-	RT	485	712
316L	SLM Solutions 125HL	95,99 – 99,30	HT - 1040°C/4h	V	RT	376	637
316L	SLM Solutions 280HL	> 99	As built	H	RT	528	639
				45°		590	699
				V		439	512
316L	Sisma MYSINT100	99,3 – 100	As built	45°	RT	505-515	650
				V		430-495	550-575
316L	Renishaw AM250	NR	As built	H	RT	554	685
316L	NR	NR	As built	-	RT	456	703
				-	250°C	376	461
				-	1100°C	-	300
				-	1200°C	-	150

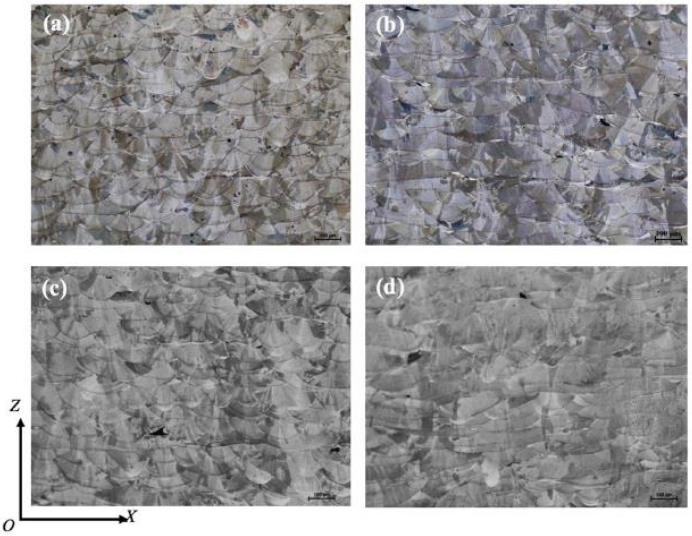

Figure 2 OM micrographs showing the microstructure of 316L samples fabricated at 200 W laser power, using different scanning strategies, (a) Meander; (b) Stripe; (c) Chessboard with 5 × 5 mm islands; (d) Chessboard with 1 × 1 mm islands. Z specifies the building direction.

Microstructural assessment of AISI304 and AISI316L grades showed that all samples are characterized by columnar grains (Figure 2, Figure 3 and Figure 4), independently of the alloy and of lased power scanning strategy (Figure 2 and Figure 3).
Some fatigue resistance results are reported in Table 2. Results show a beneficial machining operation effect, in particular in the case of high cycle fatigue (more sensitive to surface conditions or to the presence of cracks). On the contrary a negligible effect of surface roughness reduction is found in the case of low cycle fatigue tests. Microstructural characterization of both AIS 304 and AISI 316L grades allowed to state that:

- grain size does not depend on scanning strategy, once same laser power is kept constant (see Figure 2);
- grain size decreases with laser power decrease (Figure 3);
- as-built grains are show needle-like structures with medium size 500-800 nm and a high aspect ratio. These grains are oriented along different direction also if a single weld bead is considered (Figure 5).

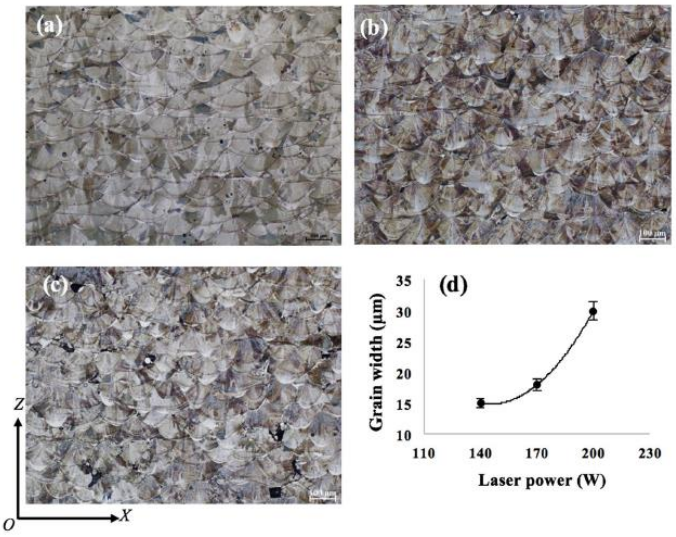

Figure 3 OM micrographs of L-PBF 316L microstructure produced at different laser powers, (a) 200 W; (b) 170 W; (c) 140 W; (d) grain width correlation to laser power values. Z specifies the building direction.

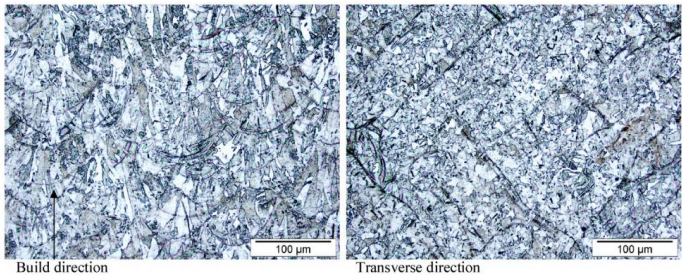

Figure 4 OM showing L-PBF 304 stainless steel microstructure, (a) along vertical cross section - heat flow effect is evident in the build direction and (b) nearly equiaxed grains in the planar direction, coincident to the layer top view.

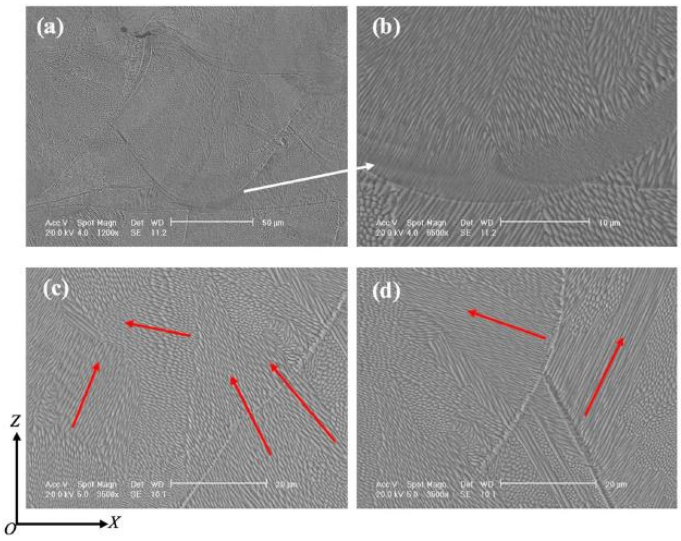

Figure 5 SEM micrographs showing the microstructure of 316L samples (laser power at 200W), (a) within a weld bead; (b) at the bottom region of (a); (c) grain structure beyond two layers; (d) grains in two adjacent weld beads. Red arrows point out grain growth direction. Z specifies the building direction.

Table 2 Fatigue endurance limits of L-PBF 316L samples, under different loading and surface conditions.

Alloy	Fatigue endurance at 10^6 cycles [MPa]	R	Surface condition	Ra [µm]
316L	130	-1	As built	13,29
316L	170	-1	Vibratory finished	1,74
316L	240	-1	Turned	1,08
316L	200	0,1	As built	10,0
316L	256	0,1	Machined	0,4
316L	269	0,1	Polished	0,1
316L	108	-1	As built	NR
316L	267	-1	Turned	NR

CONCLUSIONS

The possibility to process austenitic stainless steel grades by L-PBF has been reported. The exploitation of L-PBF technique allows to obtain relevant benefits if the following issues are required:

- artefacts weight reduction;
- easy customization;
- complex internal features manufacturing.

The above listed advantages are quite important for stainless steel grades. In this frame, the adoption of L-PBF will manifest in a large material saving and efficiency improvement in many applications including biomedical devices and power production plant. L-PBF is particularly suggested for additive manufacturing stainless steels following its capability to manufacture complex features with a good compromise in terms of costs and times, without losing low oxides contamination.

The paper showed that austenitic stainless steel alloys are satisfactorily processed by L-PBF. Further, the obtained mechanical properties target stainless steels requirements for several applications. High mechanical properties are targeted since the porosity level achieved by L-PBF is quite low and comparable to conventionally processed materials.

The analysis of listed tested alloys, relative metallurgical microstructures and tensile strengths reveals that only a few stainless steel grades are actually processed by L-PFB. This item defines the path for further researches and exploitation.

REFERENCES

1. P. Marshall: Austenitic stainless steels: Microstructure and Mechanical Properties, Elsevier Applied Science Publisher, 1984.
2. L. Viet, J. Hye-Jin: Metals, 8, 2018, 815. DOI: 10.3390/met8100815.
3. C. Xingrun, R. Xiang: Metals, 8, 2018, 1024. DOI: 10.3390/met8121024.
4. D. Hongjinng: Metals, 9, 2019, 74. DOI: 10.3390/met9010074.
5. A. Tachieva: Metals, 9, 2019, 347. DOI: 10.3390/met9030347.
6. A. Prosviryakov: Metals, 9, 2019, 218. DOI: 10.3390/met9020218.
7. R. Rufini, O. Di Pietro, A. Di Schino: Metals, 8, 2018, 519. DOI: 10.3390/met8070519.
8. A. Di Schino, P.E. Di Nunzio: Acta Metallurgica Slovaca, 23, 2017, 62-71. DOI: 10.12776/ams.v23i1.852.
9. D. Manfredi, R. Bidulsky: Acta Metallurgica Slovaca, 23(3), 2017, 276-282. https://doi.org/10.12776/ams.v23i3.988.
10. P. Petrousek et al.: Acta Metallurgica Slovaca, 25(4), 2019, 283-290. https://doi.org/10.12776/ams.v25i4.1366.
11. M. Corradi, A. Di Schino, A. Borri, R. Rufini: Constr. Build. Mater., vol. 181, 2018, 335-346. DOI: 10.1016/j.conbuildmat.2018.06.034.
12. A. Borri, M. Corradi, G. Castori, A. Molinari: Constr. Build. Mater., 211, 2019, 594. DOI: 10.1016/j.conbuildmat.2019.03.197.
13. C. Gennari, M. Lago, B. Bögre, I. Mezaros, I. Calliari, L. Pezzato: Metals. 8, 2018, 1074. DOI: 0.3390/met8121074
14. A. Di Schino, M. Longobardo, G. Porcu. G. Turconi, L. Scoppio: NACE – International Conference Series 2006, 062151-06125114.
15. G. Bregliozzi, A. Di Schino, J.M. Kenny, H. Haefke: Materials Letters, 57, 2003, 4505-4508. DOI: 10.1016/S0167-577X(03)00351-3.
16. A. Di Schino, C. Guarnaschelli: Materials Science Forum, 638-642, 2019, 3188-3193. DOI: 10.4028/www.scientific.net/MSF.638-642.3188.
17. A. Di Schino: Acta Metallurgica Slovaca, 22, 2016, 266-270. DOI: 10.12776/ams.v22i4.815
18. A. Di Schino, P. Di Nunzio. G.L. Turconi: Materials Science Forum, 558-559, 2007, 1435-1441. DOI: 10.4028/0-87849-443-x.1435.
19. L. Boulané-Petermann: Biofouling, 10(4), 1996, 275.
20. G. Bregliozzi, S.I.U. Ahmed, A. Di Schino, K.M. Kenny, H. Haefke: Tribol. Lett., 17, 2004, 697-704. DOI: 10.1007/s11249-004-8075-z.
21. A. Di Schino, L. Valentini, J.M. Kenny, Y. Gerbig, I. Ahmed, H. Haefke: Surf. Coat. Technol., 161, 2002, 224-231. DOI: 10.1016/S0257-8972(02)00557-1.
22. A. Di Schino, J.M. Kenny, G. Abbruzzese: J. Mater. Sci., 37, 2002, 5291-5298. DOI: 10.1023/A:1021068806598.
23. A. Di Schino, J.M. Kenny, I. Salvatori, G. Abbruzzese: J. Mater. Sci. , 36, 2001, 593-601. DOI: 10.1023/A:1004856001632.
24. L. Valentini, A. Di Schino, J.M. Kenny, Y. Gerbig, H. Haefke: Wear, 253, 2002, 458-464. DOI: 10.1016/S0043-1648(02)00140-0.
25. C Zitelli, P. Folgarait, A. Di Schino: Metals, 9, 2019, 731. DOI: 10.3390/met9070731.
26. Z. Brytan, M.A. Grande, M. Rosso, R. Bidulský, L.A. Dobrzański: Materials Science Forum, 672, 2011, 165. DOI: 10.4028/www.scientific.net/MSF.672.165
27. T. Kvačkaj, L. Sokolová, M. Vlado, V. Vrchovinský: High Temperature Materials and Processes, 24, 2005, 139. DOI: 10.1515/HTMP.2005.24.2.139
28. R. Bidulsky, M. Actis Grande, E. Dudrova, M. Kabatova, J. Bidulska: Powder Metallurgy, 59(2), 2016, 121-127. DOI: 10.1179/1743290115Y.0000000022.
29. C. Wang, M. Wang, J. Shi, H. Dong, H: Scripta Materialia, 58, 2008, 492. DOI: 10.1016/j.scriptamat.2007.10.053.
30. T. DebRoy, H.L. Wei, J.S. Zuback, T. Mukherjee, J.W. Elmer, J.O. Milewski, A.M. Beese, A. Wilson-Heid, De, W. Zhang: Prog. Mater. Sci., 92, 2018, 112. DOI: 10.1016/j.pmatsci.2017.10.001
31. P. Krakhmalev, G. Fredriksson, K. Svensson, I. Yadroitsev, I. Yadroitsava, M. Thuvander, R. Peng: Metals, 8, 2018, 643. DOI: 10.3390/met8080643.
32. K. Ren, Y. Chew, J.Y.H. Fuh, Y.F. Zhang, G.J. Bi, Mater. Des., 162, 2019, 80–93. DOI: 10.1016/j.matdes.2018.11.014.
33. T.M. Rodgers, J.D. Madison, V. Tikare: Comput. Mat. Sci., 135, 2017, 78-89. DOI: 10.1016/j.commatsci.2017.03.053.
34. K, Saeidi, F. Akhtar: Microstructure-Tailored Stainless Steels with High Mechanical Performance at Elevated Temperature. In Stainless Steels and Alloys; Duriagina, Z., Ed.; Intech Open, 2019, ISBN 978-1-78985-369-8.
35. L.E. Murr, S.M Gaytan, D.A. Ramirez, E. Martinez, J. Hernandez, K.N. Amato, P.W. Shindo, F.R. Medina, R.B. Wicker: J. Mater. Sci. Technol., 2012, 28. DOI: 10.1016/S1005-0302(12)60016-4.

OPEN ACCESS

ACTA METALLURGICA SLOVACA

2020, VOL. 26, NO. 1, 27-30

TECHNICAL PAPER

THE IMPACT OF INDEPENDENT VARIABLES SURFACE MACHINING DUPLEX STAINLESS STEEL ON THE FLANK WEAR

Tomasz Dyl[1], Adam Charchalis[1], Mirosław Szyfelbain[1]*

[1]Gdynia Maritime University, Faculty of Marine Engineering, Department of Marine Maintenance, Morska Street 81-87, 81-225 Gdynia, Poland

*Corresponding author: t.dyl@wm.umg.edu.pl; tel. (+48) (58) 5586-323, Faculty of Marine Engineering / Gdynia Maritime University, 81-225, Gdynia, Poland

Received: 02.08.2019
Accepted: 12.02.2020

ABSTRACT

Surface engineering is important for carried out to improve the quality of the surface layer of the material. It is important that in special applications of corrosion resistant steel, low surface roughness is obtained. Duplex stainless steel is becoming more widely used for example in the petrochemical industry or shipbuilding. Duplex stainless steel is a material classified as difficult-to-cut. It is therefore important to investigate the impact of machining parameters on the durability and wear of a cutting tool. In the paper has determined the influence of variables machining: feed rate, depth of cut, cutting speed, on the maximum tool flank wear. Surface machining was carry out with carbide tipped inserts. The criterion of the smallest roughness and the highest wear was proposed.

Keywords: duplex stainless steel; machining; flank wear; cutting tool; surface layer

INTRODUCTION

Stainless steels currently enjoy high interest shows that every year takes place a few percent increase in production. Differentiation of properties, depending on the chemical composition, microstructure, quality of the surface layer, constantly expand the application areas of these materials. A special group are ferritic-austenitic steels (duplex steels hereinafter) whose development allows to increase the durability of machine parts exposed to erosion and corrosion wear.
The combination of high mechanical strength, high corrosion resistance and relatively low cost compared to similar materials, contributed to making duplex stainless steels one of the fastest growing groups of stainless steels. The duplex stainless steels are two-phase chromium-nickel-molybdenum-iron alloys in which the proportions of the components allow optimization of the equilibrium of the volume fractions of austenite and ferrite [1-13]. Two-phase stainless steel is considered to be difficult-to-cut materials. It is therefore important to determine the cutting edge wear [4-6, 10, 14]. The wear of the turning tool occurs on all surfaces with direct contact with the workpiece material and is manifested by the loss of the tool material. The most frequently determined are indicators of wear of a turning knife-edge, such as: flank wear (VB) and distance between primary cutting edge and the most distant - crater wear (KB).

EXPERIMENTAL MATERIALS AND METHODS

Two-phase stainless steels known as duplex by treatment have physical properties similar to those of the ferritic steels, while, due to the chemical composition and resistance to corrosion are similar to austenitic steel. The experimental research was carried out in the Laboratory of Department of Marine Maintenance of the Faculty of Marine Engineering of the Gdynia Maritime University. The external cylindrical surfaces were prepared for machining process by universal turning lathe.
Cutting parameters were selected based on own research for longitudinal turning: feed rate $f = 0.1 \div 0.2$ mm/rev, depth of cut $a_p = 0.5$ mm, cutting speed $v_c = 50 \div 100$ m/min, on the maximum tool flank wear VB. Surface machining was carry out with inserts CCMT where all are made of sintered carbides of the 2025 grade.
The criterion for selecting the right cutting-tool inserts geometries for very precise machining was the arithmetic mean of the ordinates of the surface roughness profile (Ra= 0.16 ÷ 1.25 μm) and maximum tool flank wear (VB = 200 μm).
Throughout of the longitudinal turning of samples with duplex stainless steel (DIN EN 1.4410, PN-EN X2CrNiMoCuN 25-7-4, AISI 2507) (Table 1.) is usually short durability of the cutting inserts.

It is therefore important to determine the length of spiral cutting. Length of spiral cutting is a constant (L_{SC} = 9.5 m) and useful to the insert, geometry, and grade, depth of cut and material that shall be subject machined and can be calculated from the formula:

$$L_{SC} = \frac{\Pi\, D_m}{1000} \frac{l_m}{f} \tag{1}$$

where: D_m [mm] - the diameter of the workpiece in the machined surface,
l_m [mm] - length of the cutting surface,
f [mm/rev] - feed rate.

Surface roughness were measured using a profilometer Hommel Tester T1000. Parameters measurements were performed to the principles contained in ISO standards EN ISO 4287 and EN ISO 13565.

Table 1 The chemical composition and mechanical properties for samples of duplex steel DIN EN 1.4410, PN-EN X2CrNiMoCuN 25-7-4, AISI 2507

C [%]	**Cr** [%]	**Ni** [%]	**Mo** [%]	**Mn** [%]	**Si** [%]	**N** [%]	**S** [%]	**P** [%]
0.03	25.0	7.0	4.0	2.0	1.0	0.35	0.015	0.035
$R_{p0.2}$ [MPa]	**R_m** [MPa]	**R_m** [MPa]	**A_5** [%]	**HV**	**E** [GPa]	**ρ** [kg/dm^3]	**λ** [J/m·s·K]	**c_w** [J/kg·K]
550	750	1000	15	310	200	7.8	15	500

Observation and measurement of the tool wear after turning of duplex stainless steel samples was carried out using Scanning Electron Microscopy EVO MA 15 (Fig. 1). The Scanning Electron Microscope Zeiss EVO MA 15 is a device designed for examining the microstructure of solids. The device allows the imaging electron samples with a resolution of 3 nm at 30 kV. The range of possible magnification range from 5 to 1 000 000 times. The microscope enables the observation of samples with a mass up to 500 grams (at full mobility of the microscope table in XYZ directions) or up to 5 kilograms (then the table motion is limited to the XY axis directions). The microscope enables observation of samples as well as measurements of geometric quantities. The microscope is additionally equipped with an EDS analyzer. Energy Dispersive Spectrometer (EDS) XFlash 6/30 by Bruker extends the research possibilities of scanning electron microscopy with accurate and fast chemical analysis (qualitative and quantitative) of the observed surface of metallographic specimens.

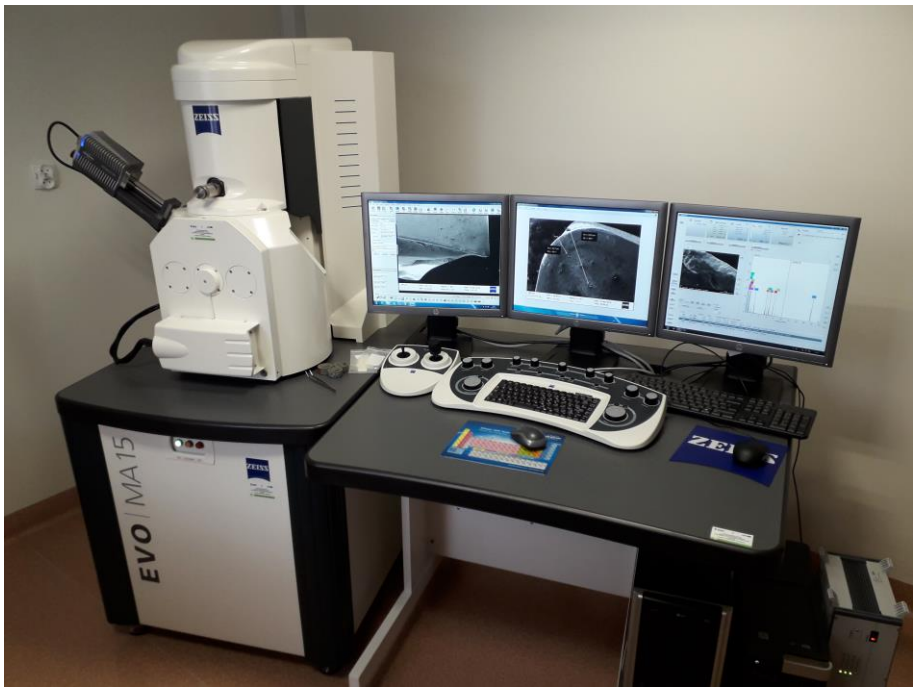

Fig. 1 Scanning Electron Microscopy EVO MA 15

RESULTS OF RESEARCH

After turning finishing duplex stainless steel, it was determined that the machining parameters affect the surface quality and knife wear. A number of roughness parameters have been defined. The smallest values of the parameter arithmetical mean deviation of the roughness profile Ra = 1.55 μm were determined after turning with the cutting insert CCMT 09T308-UM 2025 for the cutting parameters: v_c=70 m/min, f=0.2 mm/rev, a_p=0.5 mm.

Even smaller values of the Ra = 1.05 μm parameter were determined for the cutting parameters: feed rate of f = 0.1 mm/rev, with a constant cutting speed v_c = 70 m/min and depth of cut a_p=0.5mm, using a CCMT 09T304-UM cutting insert carbides of the 2025 grade with a CVD Ti(C,N)/Al_2O_3/TiN (2μm/1.5μm/2μm) [14].

The cutting inserts were characterized by the following features: cutting edge angle κ_r= 90°, tool included angle ε_r = 80°, rake angle γ= 6° and γ= 7°, flank angle α= 7°, nose radius r_ε= 0.4 mm and r_ε= 0.8 mm. For this turning tool, the smallest flank wear VB = 36 μm and crater wear KB = 18 μm was obtained (Fig.2). The surface roughness reduction ratio was equal to K_{Ra} = 3.21, which is the highest value among the presented scope of research.

The wear of cutting edge shown a view from the scanning electron microscope of the cutting inserts. The condition of used tool point surfaces was assessed using the corresponding SEM images shown in Figures 2 to 4. You can see the effects of wear on the rake face and flank. For cutting inserts with nose radius 0.8 mm the built-up edge with the clash of the major flank can be observed. However, on the cutting insert with a radius of 0.4 mm there is slight wear in the form of abrasive wear.

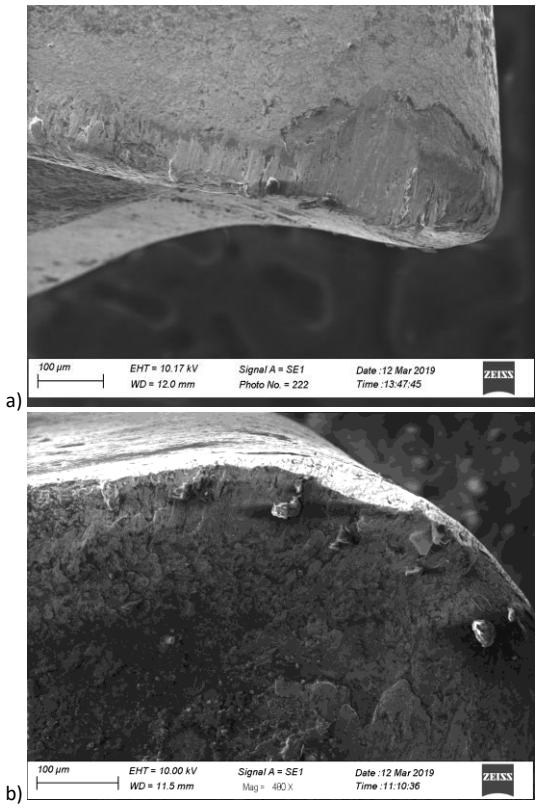

Fig. 2 The microscopic view of flank (a) and rake face (b) wear for CCMT 09T304-UM 2025 cutting insert

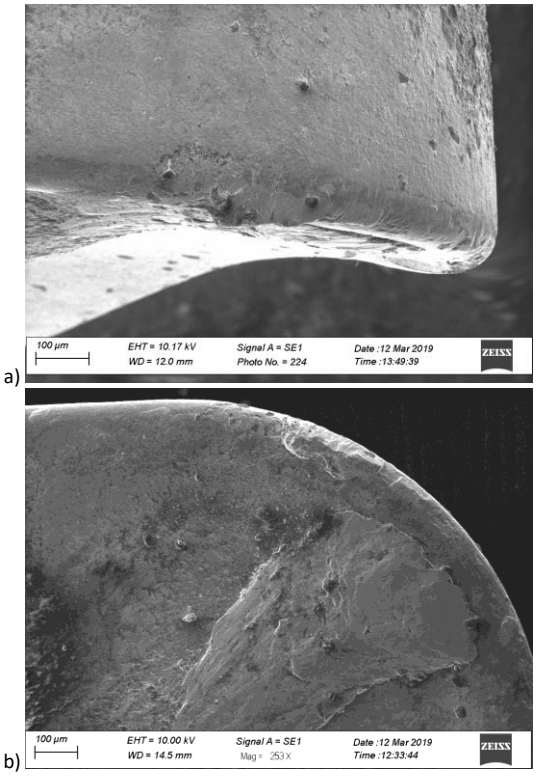

Fig. 3 The microscopic view of flank (a) and rake face (b) wear for CCMT 09T308-UM 2025 cutting insert

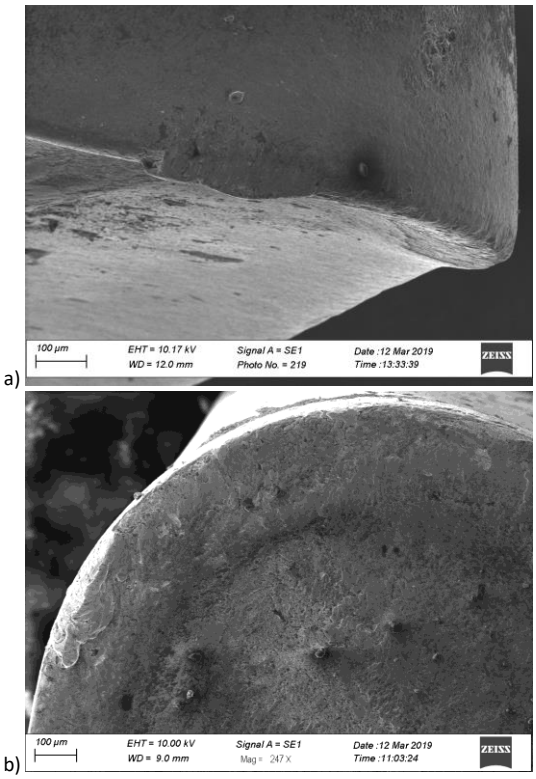

Fig. 4 The microscopic view of flank (a) and rake face (b) wear for CCMT 09T308-MM 2025 cutting insert

The wear was measured using software dedicated to microscopy and the results are shown in the Table 2. The arithmetical mean deviation of the roughness profile of the surface and maximum height of profile average value of the five measurement was shown in Table 2 and Figures 5.

Table 2 The measurements of the parameter of surface roughness for inserts used for turning cylindrical samples and example indicators of wear of a cutting edge

No samples	*Insert Shape*	*f [mm/rev]*	*v_c [m/min]*	*Rz [µm]*	*Ra [µm]*	*K_{Ra} [-]*	*VB [µm]*	*KB [µm]*
08-MM-100	CCMT 09T308-MM	0.2	100	9.19	1.93	1.71	241.7	120.9
08-MM-70		0.2	70	8.41	1.64	2.14	194.1	97.1
08-MM-50		0.2	50	11.97	2.31	1.43	292.2	146.1
08-UM-100	CCMT 09T308-UM	0.2	100	7.55	1.53	2.16	111.4	55.7
08-UM-70		0.2	70	7.44	1.55	2.13	96.4	48.2
08-UM-50		0.2	50	7.95	1.63	2.02	141.2	70.6
04-UM-70-2	CCMT 09T304-UM	0.2	70	13.85	3.03	1.09	64.7	32.3
04-UM-70-1		0.1	70	5.33	1.05	3.21	35.9	17.9

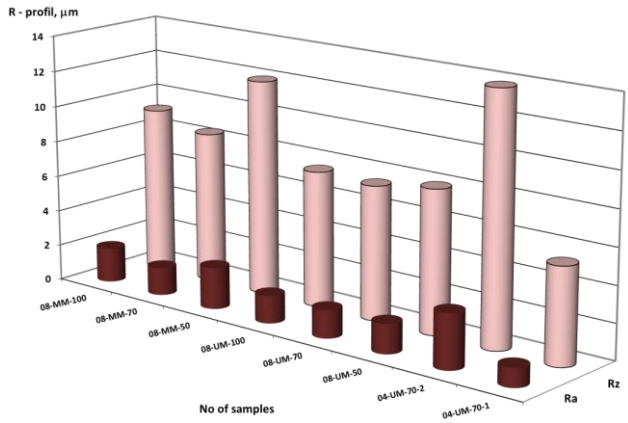

Fig. 5 The arithmetical mean deviation (Ra) and the maximum height of profile (Rz)

The criterion of the smallest roughness and the highest wear was proposed. The criterion for selecting the right cutting inserts geometries for finishing was the arithmetical mean deviation of the ordinates of the surface roughness profile, which should be within the range from 0.16 µm to 1.25 µm and the second criterion is of the maximum tool flank wear 200 µm. It can therefore be concluded that the tools used for testing meet the wear criterion. The cutting tools meet the criterion with the exception of insert shape CCMT 09T308-MM (Fig. 6).

After the analysis experimental research can be defined that to achieve a reduction in surface roughness after the longitudinal turning finishing of the samples of the duplex stainless steel, should be use with a constant cutting speed v_c = 70 m/min and depth of cut a_p = 0.5 mm for feed rate f = 0.1 mm/rev for cutting insert CCMT 09T304-UM 2025 where is the smallest flank wear VB = 36 µm.

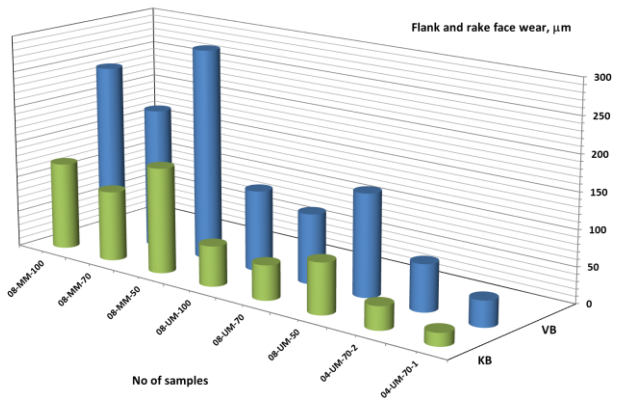

Fig. 6 The flank wear (VB, mm) and rake face wear (KB, mm) for different inserts

Figure 7 shows the EDS analysis showed that this is a build-up of duplex steel. It can be seen that determined by EDS analysis of the presence of alloying elements typical of two-phase stainless steel.

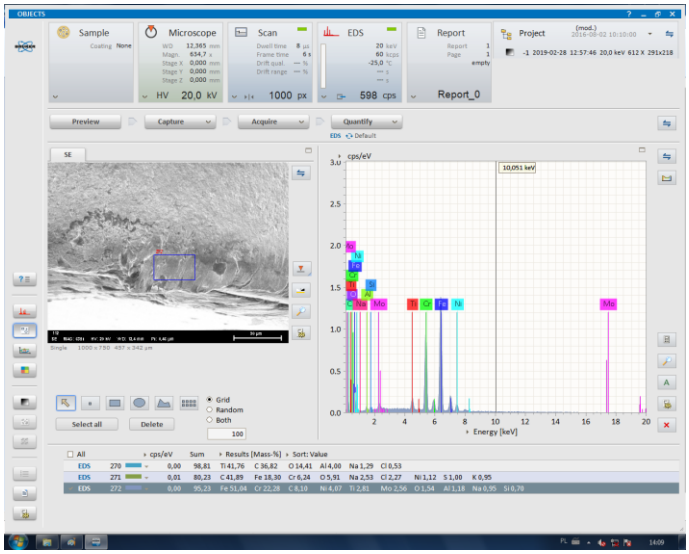

Fig. 7 The flank wear for CCMT 09T308-UM 2025 cutting insert with an EDS analyzer

CONCLUSION

In the paper were presented the influence of the geometry of the cutting edge and machining parameters of duplex stainless steel after finishing turning on the surface roughness reduction ratio and flank wear.

The turning of external cylindrical surfaces of duplex stainless steel in was carried out by inserts shape CC09T3 of the grade 2025 with applied coating by CVD method.

Turning the duplex steel to obtain a smooth surface should be carried out using the cutting insert for the nose radius r_ε= 0.4 mm with cutting parameters: feed rate f = 0.1 mm/rev, cutting speed v_c = 70 m/min, depth of cut a_p = 0.5 mm.

There arithmetical mean deviation of the roughness profile of the surface after turning is equal Ra = 1.05 µm. Therefore, for the finishing of duplex steel, it can be proposed insert type CCMT 09T304-UM 2025, where is the smallest flank wear VB = 36 µm and crater wear KB = 18 µm and surface roughness reduction ratio K_{Ra} = 3.21 was equal.

Only one insert CCMT 09T304-UM 2025 meet the quality criterion, where Ra parameter is less than the value of 1.25 µm and the wear criterion of the maximum tool flank wear VB = 200 µm.

REFERENCES

[1] A. Armas, S. D. Moreuil: Duplex Stainless Steels. UK&USA: ISTE Ltd. John Wiley&Sons Inc. 2009.

[2] T. Burakowski, T. Wierzchoń: Surface Engineering of Metals: Principles. Equipment. Technologies. Materials Science & Technology. CRC Press LLC. London. New York. Washington D.C. 1999.

[3] J. Charles: Duplex stainless steels, a review after DSS'07 held in Grado, Revue de Metallurgie, 105, 2008, 155-171.

[4] T. Dyl: The influence of the geometry of the cutting edge and machining parameters of duplex cast steel after turning, Journal of KONES, 25, 2018, 75-82, doi:10.5604/01.3001.0012.4778.

[5] G. Królczyk, P. Niesłony, S. Legutko: Determination of tool life and research wear during duplex stainless steel turning, Archives of Civil and Mechanical Engineering, 15(2), 2015, 347-354, https://doi.org/10.1016/j.acme.2014.05.001.

[6] G. Królczyk, P. Niesłony, S. Legutko, S. Hloch, I. Samardzic: Investigation of selected surface integrity features of duplex stainless steel (DSS) after turning, Metalurgija, 54, 2015, 91-94, https://hrcak.srce.hr/126702.

[7] J. Nowacki: Duplex steel and its weldability, WNT, Warszawa 2009, (in Polish).

[8] J. Paro, H. Hanninen, V. Kauppinen: Tool wear and machinability of HIPed P/M and conventional cast duplex stainless steels, Wear, 249, 2001, 279-284, https://doi.org/10.1016/S0043-1648(01)00570-1.

[9] Q. Ran, J. Li, Y. Xu, X. Xiao, H. Yu, L. Jiang: Novel Cu-bearing economic al 21Cr duplex stainless steels, Materials and Design, 46, 2013, 758-765, https://doi.org/10.1016/j.matdes.2012.11.017.

[10] R. Starosta, T. Dyl: Finishing of flame sprayed Ni-Al coatings, estimate of CBN inserts wear, Tribologia, 4, 2011, 245-252.

[11] R. Starosta, T. Dyl: Surface engineering, Publisher of the Gdynia Maritime University, 2008, (in Polish).

[12] G. Stradomski: The Analysis of AISI A3 Type Ferritic - Austenitic Cast Steel Crystallization Mechanism, Archives of Foundry Engineering, 17, 2017, 229-233, https://doi.org/10.1515/afe-2017-0120.

[13] G. Stradomski: The impact of the morphology of the sigma phase on shape properties of steel and cast steel duplex, Czestochowa University of Technology, Czestochowa, 2016, (in Polish).

[14] [02.02.2020] Tools for metal cutting, Turning tools, Turning inserts and grades for stainless steel, CoroTurn®107 grade:2025, Sandvik Coromant, 2020, http://www.sandvik.coromant.com/en-us/products/pages/tools.aspx.

OPEN ACCESS

ACTA METALLURGICA SLOVACA

2020, VOL. 26, NO. 1, 31-33

TECHNICAL PAPER

PREDICTION OF FATIGUE CRACK GROWTH DIAGRAMS BY METHODS OF MACHINE LEARNING UNDER CONSTANT AMPLITUDE LOADING

Oleh Yasniy[1)], Iryna Didych[1)], Yuri Lapusta[2)]

[1)] *Ternopil Ivan Pul'uj National Technical University, Faculty of Computer-Information Systems and Software Engineering, Ternopil, Ukraine*

[2)] *University Clermont Auvergne, CNRS, SIGMA Clermont, Institut Pascal, F-63000 Clermont-Ferrand, France*

**Corresponding author: iryna_didych@ukr.net; tel.: +380972272074, Faculty of Computer-Information Systems and Software Engineering / Ternopil Ivan Pul'uj National Technical University, 46001, Ternopil, Ukraine*

Received: 03.01.2020
Accepted: 03.02.2020

ABSTRACT

Important structural elements are often under the action of constant amplitude loading. Increasing their lifetime is an actual task and of great economic importance. To evaluate the lifetime of structural elements, it is necessary to be able to predict the fatigue crack growth rate (FCG). This task can be effectively solved by methods of machine learning, in particular by neural networks, boosted trees, support-vector machines, and *k* -nearest neighbors. The aim of the present work was to build the fatigue crack growth diagrams of steel 0.45% C subjected to constant amplitude loading at stress ratios $R = 0$, and $R = -1$ by the methods of machine learning. The obtained results are in good agreement with the experimental data.

Keywords: fatigue crack growth, stress intensity factor, stress ratio, neural network, lifetime, machine learning

INTRODUCTION

Methods of strength and durability evaluation of the responsible structural elements often need the complicated calculations. Therefore, it is important to learn how to solve the problems of fracture mechanics by methods of machine learning, in particular, neural networks (NN), support-vector machines (SVM), *k* - nearest neighbors and boosted trees, which allow to achieve high accuracy of solutions [1 – 4] .

The structural elements are often fractured by fatigue, gradually accumulating damage. It is possible to observe a small crack which grows under loading. The fatigue crack is formed mainly at the stress concentrator, that is, the place of damage, which weakens the cross-section of the material. The crack grows as long as the material is able to withstand the loading. Therefore, the basic factors that influence the strength of structural elements are the surface defects of the parts, temperature and the environment during operation, the nature of loading and loading conditions [5].

It is known that, the basic parameters characterizing the fatigue crack growth (FCG) rate da / dN are the stress intensity factor ΔK (SIF) and the stress ratio R [6 – 9]. The fatigue crack growth diagram is usually built in double logarithmic coordinates $lg\ da/dN - lg\ \Delta K$. It has the form of an S-shaped curve limited on the left by the threshold SIF range ΔK_{th}, and on the right by the critical SIF ΔK_{fc} (cyclic fracture toughness). The threshold SIF ΔK_{th} is determined experimentally. It is an important characteristic of material resistance to fatigue fracture. The diagram consists of three regions: region *I* corresponds approximately to the rate $da / dN \approx 10^{-10}...10^{-8}$ *m/cycle*, in which the rate of the FCG increases significantly with a slight change of ΔK. Region *II* has the form of a straight line. The rate in this region is in the range of $10^{-8}...10^{-6}$ *m/cycle*. In particular, it is considered that here the crack grows evenly for each loading cycle. Region *III* is characterized by accelerated FCG and corresponds the values of $da/dN > 10^{-6}$ *m/cycle* [5]. At high SIF values, the rate of crack growth is extremely high.

P. Paris and F. Erdogan found out that the FCG rate for metallic materials can be determined by the SIF [10]. In particular, the formula obtained by them describes only the second region of the fatigue fracture diagram and does not take into account the influence of the stress ratio R on the FCG rate [11].

It is known that, with increasing R the FCG rate increases [12-13]. Therefore, the Walker's equation [2, 14] is used to describe the FCG rate taking into account the stress ratio R. However, these models don't take into account the variable regions of FCG. The Forman's equation [15-16] is used to describe the FCG curve with high ΔK values. NASGRO model can describe all parts of the FCG diagram [17].

MATERIAL AND METHODS

Machine learning: Background and Modeling

Progress of modern technology, in particular, high demands for accuracy and efficiency, have led to the creation of methods that solve a number of important tasks. Therefore, neural networks, support-vector machines, *k* - nearest neighbors, boosted trees are powerful algorithms of supervised learning, which can be used to predict FCG.

NN consist of a very large, though the finite, number of items that form the input layer, one or more hidden layers of computational neurons, and one output layer. The input signal is transmitted over the network in the direction from layer to layer [18]. Such networks are usually called multilayer perceptrons, which quite accurately solve different tasks. NN determines the relationship coefficients between neurons, whereas the computational power of a multilayer perceptron is in its ability to learn on its own experience and the backpropagation algorithm. The idea of this algorithm is based on an error correction. The basic parameters of NN are its topology, algorithm of training and the functions of the neurons activation. In the current study, the sum of squares error function (SOS) was chosen and the training method was Broyden–Fletcher–Goldfarb–Shanno (BFGS) [19-22]. The stop parameter of learning network was number of epochs, which in this study was equal to 1000.

The boosted trees algorithm reflects the natural thinking of human processes while making a decision [23]. The data obtained by building and using boosted trees are logical and easy for visualizing and interpreting. The algorithm of building the boosted trees structure consists of the creating and cancellation stages of trees. In creating trees, one chooses the criteria of splitting and termination of learning, whereas in the course of trees cancellation, some branches are removed. The boosted trees method is used when the results of one decision influence the next, in particular, for making consistent decisions.

The ideas of the methods of support-vector machines and *k*-nearest neighbors are the simplest [24]. In the first method, the data are presented as points in the space. The training data are split into two categories. The training algorithm creates a model attributing new data to a certain category. Geometrically, it looks as if we are trying to draw a straight line centrally between two sets. The nearest to this straight line points are the support vectors. The support-vector machines method, as any method of machine learning, has many parameters. In this case, the basis objects are the regularization parameter, the loss function, which treats as errors only predicted values deviating from the actual values by a distance greater than ε, and the kernel parameter γ. As the kernel function, the radial basis

function (RBF) is used. The method of *k*-nearest neighbor assigns a new object to the class that is the most common over *k*-nearest neighbors of the training sample. The distance between *k*-nearest neighbors is usually chosen as Euclidean. The aim of the learning process is to minimize the loss function, which should decrease. In the current study, the loss function was chosen as the mean squared error (MSE) [4]:

$$E = \frac{1}{n}\sum_{i=1}^{n}(y_{prediction} - y_{true})^2 \quad (1.)$$

where: $y_{prediction}$ [m/cycle] - the predicted element of sample
y_{true} [m/cycle] - the true value of the sample element
n - the volume of the training sample

Therefore, to train the networks one needs a dataset that contains as many observations as possible. In particular, it is advisable to experiment with different networks topologies to avoid getting the erroneous result in the case, if the learning process has found the local minimum of the target loss function. Therefore, if in the next experiment one observes underfitting, that is, the network issues a dissatisfactory result, we should try adding a new hidden layer. On the other hand, if the error started to grow, that is, overfitting occurs, one should try to remove one or more hidden layers.
The prediction error was Mean Absolute Percent Error (MAPE):

$$MAPE = 100\% \cdot \frac{1}{n}\sum_{i=1}^{n}\frac{|y_{true} - y_{prediction}|}{|y_{true}|} \quad (2.)$$

Experimental material(s) and methods

During the operation, a railway axle undergoes static and cyclic loading, including random loading, bending, as well as corrosive action of environment and climate temperatures.
The FCG rate in axle steel was predicted by methods of machine learning according to the experimental data of FCG obtained for 0.45% *C* steel and stress ratios R = 0, –1 [25]. The sample consisted of 200 elements, 70% of which were chosen randomly for the training sample and 30% were left for estimating the quality of predictions. The input parameters were the SIF range ΔK and the stress ratio R. The FCG rate da/dN under regular loading for the stress ratios R = 0, –1 was chosen as the output parameter. The input and output parameters were normalized using the decimal *log* function to decrease the prediction error.

RESULTS AND DISCUSSION

The dependences of the experimental FCG rates da/dN_{exp} on the predicted FCG values da/dN_{pred} for R = 0, –1 are shown in Fig. 1.

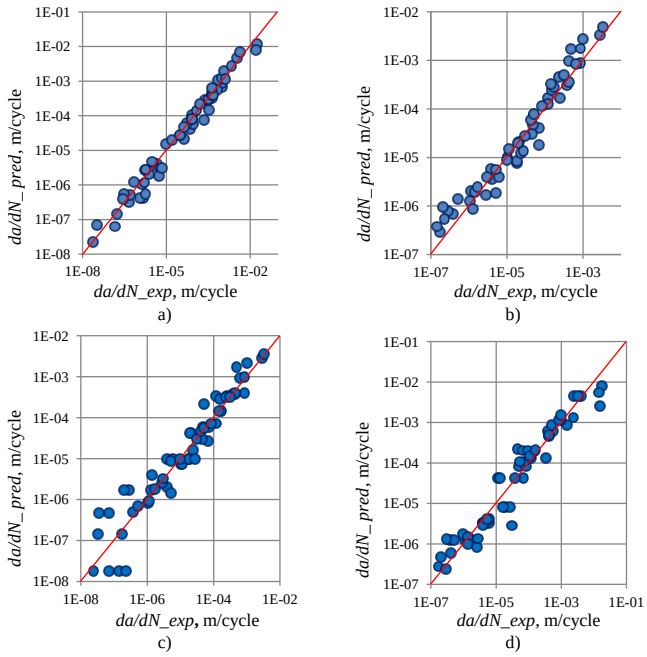

Fig. 1 The experimental (da/dN_{true}) and predicted (da/dN_{pred}) FCG rates for R = 0, –1 by methods of neural networks (*a*), support-vector machines (*b*), *k*-nearest neighbors (*c*), boosted trees (*d*)

There were built the experimental and predicted dependences of the FCG rate da/dN on the SIF range ΔK for R = 0, –1 using the methods of machine learning (Fig. 2).

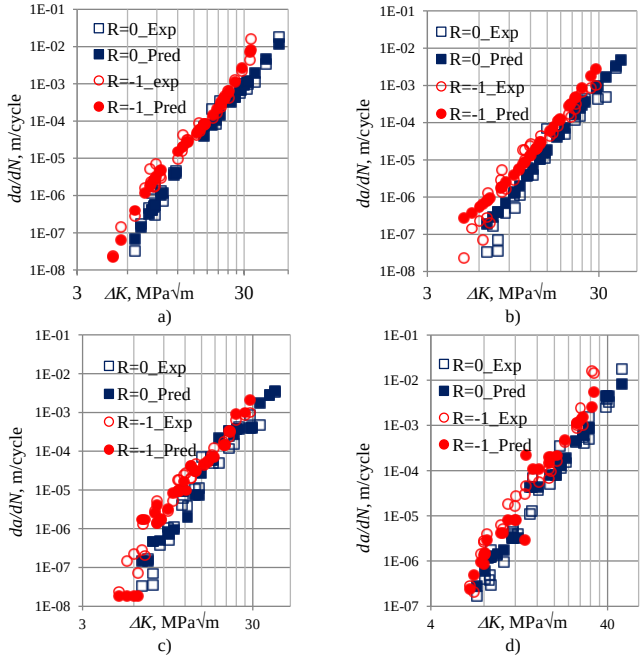

Fig. 2 The experimental da/dN_{true} and predicted da/dN_{pred} dependences of FCG rate on the KIN ΔK for R = 0, –1 by the methods of neural networks (a), support-vector machines (b), *k* - nearest neighbors (c), boosted trees (d)

The parameters of the constructed neural networks, support-vector machines, *k* - nearest neighbors and boosted trees are summarized in Tables 1−3.

Table 1 Parameters of Neural Network and Boosted trees

Stress ratio	Name of network	Function of hidden activation	Function of output activation	Number of repetitions (for boosted trees)
R = 0, –1	MLP 2-6-1	Logarithmic	Exponential	200

Table 2 Parameters of Support-Vector Machines

Stress ratio	Regularization parameter	Insensitive loss function ε	Kernel Parameter γ	Number of support vectors
R = 0; –1	10	0,1	0,5	30 (bounded by 19)

Table 3 Parameters of *k* -Nearest Neighbors

Stress ratio	Number of nearest neighbors	Distance
R = 0; –1	1	Euclidean

The error of the NN method for the test sample is 4.5%, the support-vector machines is 5.5%, the *k* - nearest neighbors is 5.5% and the boosted trees is 6.7%.

CONCLUSION

The predicted FCG rate data are in good agreement with the experimental ones. In the present study, the NN prediction accuracy is 95.5%, which is the best among the applied methods. Support-vector machines, *k* - nearest neighbors, and boosted trees also show good results in terms of accuracy. The methods of machine learning are powerful and efficient tools which allow evaluating the FCG behavior.

REFERENCES

[1] O. P. Yasnii, O. A. Pastukh, Yu. I. Pyndus, N. S. Lutsyk, I. S. Didych: Materials Science, 54(3), 2018, 43–48. https://doi.org/10.1007/s11003-018-0189-9

[2] I. Didych, O. Pastukh, Yu. Pyndus, O. Yasniy: Acta Metallurgica Slovaca, 24(1), 2018, 82-87. http://dx.doi.org/10.12776/ams.v24i1.966

[3] J. R. Mohanty, B. B. Verma, D. R. K. Parhi, D. R. Ray: Archives of Computational Materials Science and Surface Engineering, 1(3), 2009, 133–138.

[4] R. M. V. Pidaparti, M. J. Palakal: Journal of Aircraft, 32(4), 1995, 825-831. https://doi.org/10.2514/3.46797

[5] Yasnii P.V.: *Plastychno deformovani materialy: vtoma i trishchynotryvkist* [Plastically deformed materials: fatigue and fracture toughness], first ed., Lviv: Svit, 1998. [in Ukrainian]

[6] M. Klesnil, P. Lukas: Materials Science and Engineering, 9, 1972, 231-240. https://doi.org/10.1016/0025-5416(72)90038-9

[7] D. Kujawski, F. Ellyin: Engineering Fracture Mechanics, 28(4), 1987, 367-378. https://doi.org/10.1016/0013-7944(87)90182-2

[8] S. Dinda, D. Kujawski: Engineering Fracture Mechanics, 71(12), 2004, 1779-1790. https://doi.org/10.1016/j.engfracmech.2003.06.001

[9] D. Kujawski: International Journal of Fatigue, 23(8), 2001, 733-740. https://doi.org/10.1016/S0142-1123(01)00023-8

[10] P. C. Paris, F. A. Erdogan: Journal of Basic Engineering, 85(4), 1963, 528−533. https://doi.org/10.1115/1.3656900

[11] A. F. Siqueira, C.A.R.P. Baptista, O.L.C. Guimarães, C.O.F.T. Ruckert: Procedia Engineering, 2(1), 2010, 1905-1914. https://doi.org/10.1016/j.proeng.2010.03.205

[12] C. M. Hudson: NASA TN D-5390, 1969, 34.

[13] C. M. Hudson, J. T. Scardina: NASA TMX- 60125, 1967, 24.

[14] W. Zhang, H. Liu, Q. Wang, J. A. He: Materials (Basel), 10(7), 2017,689. https://doi.org/10.3390/ma10070689

[15] E. Richey III, A.W. Wilson, J.M. Pope, R.P. Gangloff: *Computer modeling the fatigue crack growth rate behavior of metals in corrosive environments*, first ed., NASA Contractor Report 194982, Virginia, 1994

[16] C. Proppe, G. Schuëller: In ICF10, Honolulu, USA, 2001

[17] [06.07.2017], www.nasgro.swri.org

[18] S. Haykin: *Neural Networks: A Comprehensive Foundation*, 2nd ed., Prentice Hall, 1999

[19] D. N. Richard: *Applied regression analysis*, third ed., John Wiley & Sons, New York, 1998

[20] I. Goodfellow, Y. Bengio, A. Courville: *Deep Learning*, The MIT Press, 2016

[21] Ph. D. Wasserman: *Neural Computing: Theory and Practice*, New York: Coriolis Group (Sd), 1989

[22] K. Gurney: *An introduction to neural networks*, first ed., Taylor & Francis Group, London, 1997

[23] T. M. Mitchell: *Machine learning*, McGraw-Hill Science/Engineering/Math, London, 1997

[24] A. Smola, S.V.N. Vishwanathan: *Introduction to Machine Learning*, Cambridge University Press, 2010

[25] O. Yasniy, Y. Lapusta, Y. Pyndus, A. Sorochak, V. Yasniy: International Journal of Fatigue, 50, 2013, 40–46. https://doi.org/10.1016/j.ijfatigue.2012.04.008

OPEN ACCESS

ACTA METALLURGICA SLOVACA

2020, VOL. 26, NO. 1, 34-36

TECHNICAL PAPER

HYBRID SOLUTION FOR TWO-WAY INDUCED SHAPE MEMORY ACTUATOR

Girolamo Costanza[1*], *Maria Elisa Tata*[2]

[1] Industrial Engineering Department, University of Rome Tor Vergata, Via del Politecnico, 1- 00133, Rome, Italy
[2] Computer Science and Civil Engineering Department, University of Rome Tor Vergata, Via del Politecnico, 1- 00133, Rome, Italy

*Corresponding author: costanza@ing.uniroma2.it; Industrial Engineering Department, University of Rome Tor Vergata, Via del Politecnico, 1- 00133, Rome, Italy

Received: 06.02.2020
Accepted: 20.03.2020

ABSTRACT

The actuation capability and the reliability of hybrid composites activated by shape memory alloys (SMA) are discussed in this work. The manufacturing of compact and safe actuators has been possible employing thermo-activated SMA which allows the polymer-based matrix to undertake many geometries. Different technological procedures are proposed for the manufacturing of this type of composites and the problems related to the production of such elements are discussed too. The adoption of non-metallic materials as deformation recovery elements, even if at present they do not allow a complete reversibility of the imposed deformation, represent an interesting research field, due to their properties of lightness, flexibility and low cost.

Keywords: hybrid actuators; shape memory alloys; smart materials

INTRODUCTION

Among the smart materials shape memory alloys hybrid composites play an important role thanks to their mechanical properties and their ability to act as the thermal sensors or actuators. Indeed they can modify the geometry according to the temperature increase and they are able to recover the original position after cooling. The working principle of such materials is based on an active element, sensible to the temperature changes, inserted in a matrix of polymeric material which represents the element used for the shape recovery. As active element Ni-Ti shape memory alloys are usually adopted in form of sheets or springs. Ni-Ti alloys are widely employed in the field of thermo-activated sensors and actuators, thanks to their stability and strength when subjected to bound recovery. Ni-Ti wires are able to recover up to 10% strain in uniaxial tensile tests and also higher values in form of springs. They show a satisfactory compromise in terms of costs, weight reduction and dimensions of the activation systems. In this work the main technological problems, arisen during the manufacturing of an hybrid-composite actuator and solved, are reported. Many actuators have been designed, built up and checked in order to test the shape recovery performance [1]. Shape memory alloys show three different properties depending on the temperature and on the thermomechanical treatment they have been subjected to: One Way Shape Memory Effect (OWSME), Two Way Shape Memory Effect (TWSME) and Super Elasticity (SE) [2-3]. The shape memory mechanism is based on a reversible thermoelastic martensitic transformation. During cooling of SMA element, from a temperature such that its structure is completely austenitic, the formation of martensite will be evidenced. This phase grows inside the austenitic matrix in the form of lamellae that cause a plastic arrangement of the surrounding matrix (Fig. 1).

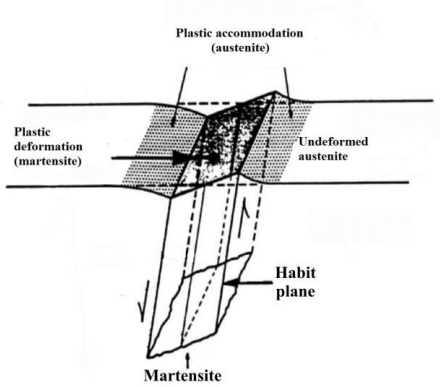

Fig. 1 Sketch of the martensitic transformation

During the subsequent heating of the alloy the recovery of the deformation will be caused by the transformation of martensite into austenite (OWSME). The two-way shape memory effect is instead completely similar to the previous one with the difference that the alloy is able to recover a different shape also during cooling (Fig. 2).

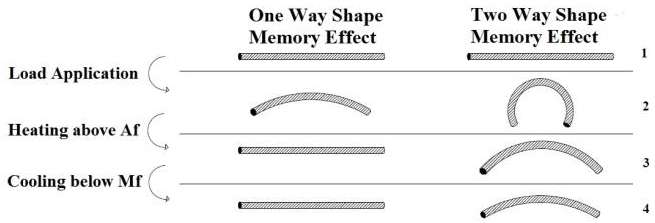

Fig. 2 Comparison between OWSME and TWSME

Finally in the superelastic alloys heating is not required for shape recovery: they are able to recover the deformation just upon stress removal (Fig. 3). This phenomenon is evident at temperatures in which the austenite is the only stable phase. The properties of the SMA just described are exploited in different fields: in the biomedical field through the realization of self-expanding stents and filters, in the safety field and fire prevention they are used in the sprinklers construction and valves, or in the civil engineering sector [4-5]. Superelastic alloys are also employed as dampers of seismic stresses, through the realization of reinforcements for masonry structures [6-7].

Fig. 3 Temperature ranges for Shape Memory Effect and Superelastic Effect

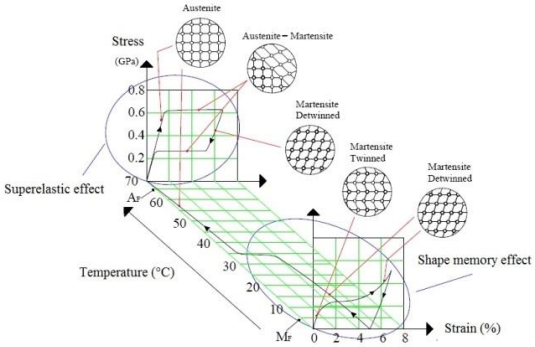

SMA's with two-way shape memory effect allow more interesting applications than a one-way memory effect one, and it is for this reason that this property is

investigated in order to understand the complex mechanisms occurring during the phase transformations [8]. However, many studies and experiments have shown that the TWSME is very unstable and tends to deteriorate after a few stress cycles. For this reason they can't be employed in industrial applications in which many activation cycles are required [9-10]. In the solar sail field a possible application has been identified too [11-15], solar power production [16] as well as in aircraft wings [17-20] and in general space applications [21-22].

MATERIAL AND METHODS

In this work it has been decided to overcome the problem of the stability of TWSME alloys by coupling OWSME alloys that allow to recover the deformation imposed, with a polymeric sheet. In this way a mechanically induced two-way memory effect has been obtained. One of the most used techniques to study shape memory alloys, in order to characterize their behavior and observe the phase stability as a function of temperature, is the resistivity test [23]. Through this technique, used with Nickel-Titanium samples, it has been possible to determine the transformation temperatures and the beginning of the shape recovery for the actuator. The temperatures characterizing a shape memory alloy (Fig. 3) are the Austenite start (As) temperatures, at which the formation of the austenitic phase begins, to which the start of the shape recovery is associated, and the Austenite finish temperature (Af), limit beyond which the alloy is completely transformed into austenite. Similarly for the martensitic phase it is possible to identify the characteristic temperatures: the martensite start temperature (Ms), in correspondence of which the formation of martensite begins while cooling within the austenitic matrix and the martensite finish temperature (Mf), temperature below which the martensitic transformation is completed. With reference to the fig. 4 it is also possible to detect the formation of a third phase in addition to those already mentioned when the alloy is cooled. This is the so-called R phase, characterized by a crystalline structure with a rhombohedral lattice, which grows as an intermediate transition phase between austenite and martensite and whose behavior and properties are still being studied.

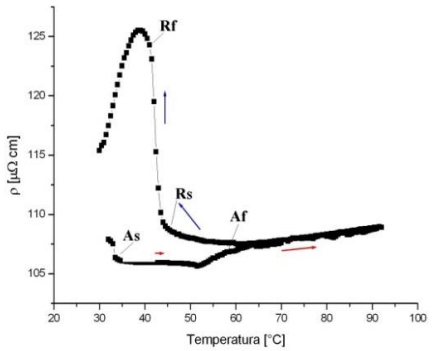

Fig. 4 Rs and Rf temperatures of rhomboedral phase on cooling (resistivity test on Ni-Ti shape memory alloys)

However, under appropriate training conditions of the alloy it has been observed that the TWSME effect is associated with the phase R in cooling, regulated by the arrangement and the number of dislocations induced in the material. The R phase also appears in heating under appropriate conditions of fatigue of the material. One of the advanced hypothesis is that this phenomenon can be associated to the degradation of the SME as this phase transformation is not associated with a thermoelastic transformation. This type of analysis provides important data on the state of the alloy, its activation temperatures, fatigue behavior and relative degradation of the shape recovery with the number of cycles [3].
The actuator proposed in this study works according to the principle of a bending sheet and is based on an active element made of NiTi alloy wire of 1.5 mm rolled to obtain a 0.5 mm thick tape, heat treated at 500° C for 5 minutes, in order to give the actuator its operational shape, and finally water quenched. The sheet thus obtained is inserted inside a 3 mm thick epoxy resin matrix, which is the element able to move back the actuator to its original configuration while the device is cooled down (fig. 5 a, b).

Fig. 5 top) undeformed – bottom) deformed shape of the NiTi sheet inside the resin matrix. Both pictures illustrate the conditions after a few activation cycles, thus involving not complete flatness of the starting configuration, increasing with the number of activation cycles.

The main purpose of the first series of samples was to test the real capacity of the resin to recover the deformation imposed by the active element. Therefore no reinforcements have been used in the matrix at this preliminary stage. The injection of the resin into the mold was followed by polymerization, with the sheet under a moderate tensile stress, in order to keep it in place during the resin polymerization (fig. 6).
After extracting the sample from the mold, it has been possible to activate the element by placing it in hot water at 60° C, temperature higher than Af in the free shape recovery, and performing several heating-cooling cycles. Fig. 5b shows the maximum deformation reached by the actuator in the hot stage and the maximum deformation recovered by cooling. A loss of the mechanical characteristics of the resin was observed due to the overcoming of the glass transition temperature during the test.

Fig. 6 Shape memory sheet under polymerization in the tensile machine

An attempt has been made to reduce the polymerization times of the resin with a heat treatment at 100° C for 2 hours. It has been decided to move in this direction in the attempt to compensate for the loss of the mechanical characteristics of the resin, providing a more rigid structure. However, the treatment causes stiffening and weakening of the matrix only at room temperature, while during the test the same behavior occurred as in the previous case.
With the aim of compensating for the loss of stiffness of the resin it has been attempted to make samples with a fiberglass reinforcement inside the matrix arranged as shown in fig. 7. At the end of a 4-day polymerization period the samples have been tested, and the composite structure immediately exhibited some problems to reach the operative configuration due to an excessive stiffening of the matrix caused by the high number of fibers placed on the upper side (tension). Therefore, a part of these has been removed, leaving the arrangement of the fiber on the compressed side unchanged. At a subsequent test, the actuator has broken down because the fibers stressed under compression, on the lower side have caused failure in the resin during the deformation.
The successive step has been the analysis of the behavior of the dispersion inside the matrix of a fine and homogeneous distribution of glass microspheres (100 μm average diameter), in order to obtain an improvement of the mechanical characteristics. The preparation of the samples has been preceded by a series of analyses on the sedimentation dynamics of the spheres inside the matrix in order to avoid deposition on the bottom side due to the difference in density between

resin and spheres (fig. 8). The samples thus obtained have been tested; no substantial improvements in the mechanical characteristics have been detected in comparison with the unreinforced resin although they are characterized by a good recovery of the deformation and stability for several activation cycles.

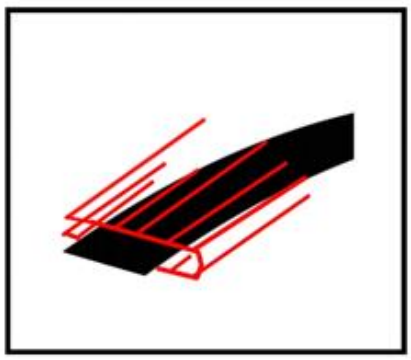

Fig. 7 Sketch of the shape memory sheet with fiber glass reinforcement inside the matrix

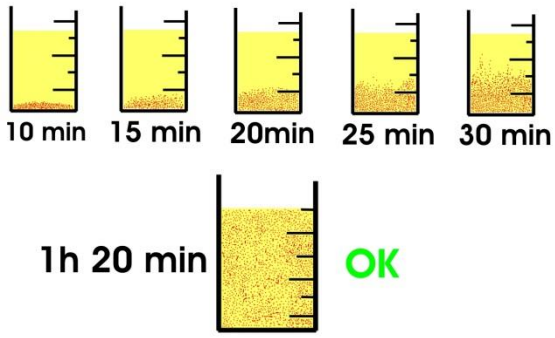

Fig. 8 Sedimentation analysis of the glass microsphere inside the resin

DISCUSSION

The experimentation carried out, in order to realize a hybrid SMA / polymer actuator, has highlighted some problems. It is possible to obtain a good stability for applications at high activation cycles, even if the shape recovery at room temperature is partial. The result of a stable mechanically induced two-way shape memory effect can be achieved. This aspect is important because the main limit of the TWSME is that the shape "memorized" at lower temperature is not stable and is gradually loss as the activation cycles proceed.

CONCLUSIONS

In order to overcome the problems associated with the degradation of the intrinsic TWSME of the alloy, with good precision and operational stability, hybrid SMA / polymer actuator have been investigated. The solution based on the use of only resin without any kind of reinforcement showed partial shape recovery. One of the possible applications of the hybrid SMA/polymer actuator could be in fire protection, starting from the concept of an actuator associated with a optic fiber to be used in the tunnels [24]. The adoption of hybrid technologies can be developed in a solution which can be reset in case of activation due to fire detection or periodically in case of test. Mounted together with a fiber cable, the SMA element would be able to bend it if the activation temperature exceeds the safety value and causing an attenuation in the signal passing through the cable is able to generate the alarm. On very long installations it is possible, by appropriately spacing the sensors, to obtain accurate informations about the position in which the alarm was generated and to observe the direction and speed of propagation of fire. The use of non-metallic materials as deformation recovery elements, even if at present they do not allow a complete reversibility of the imposed deformation, represent an interesting research field, due to their properties of lightness, flexibility, low cost.

REFERENCES

[1] Z.G. Wei, C.Y. Tang, W.B.Lee: Journal of Materials Processing Technology, Vol. 69, 1997, No. 1-3, p. 68-74, DOI:10.1016/S0924-0136(96)00041-6
[2] G. Costanza, M.E. Tata, C. Calisti: Sensors and Actuators A: Physical, Vol. 157, 2010, No. 1, p. 113-117, DOI:10.1016/j.sna.2009.11.008
[3] G. Costanza, M.E. Tata, R. Libertini: Effect of temperature on the mechanical behavior of Ni-Ti Shape Memory Sheets, Proceedings of the TMS2016 Annual Meeting, Nashville, TN USA, 2016, 433-439.
[4] Simon Nitinol Filter™, 2002, C.R. Bard Inc.
[5] A.D. Johnson, R. Gilbertson, V. Martynov, Patent US 2008/051949.
[6] L. Janke, C. Czaderski, M. Motavalli, J. Ruth: Materials and Structures, Vol. 38, 2005, No. 5, p. 578-592, DOI: 10.1007/BF02479550
[7] H. Wu., L. Mc Schettky: Industrial applications for shape memory alloys, International conference on shape memory alloys and superelastic technologies, Pacific Grove, CA USA, 2000, 171-182.
[8] Z.G. Wang, X.T. Zu, J.Y. Dai, P. Fu, X.D. Feng: Materials Letters, Vol. 57, 2003, No. 9, p. 1501-1507, DOI: 10.1016/S0167-577X(02)01014-5
[9] J. Uchill, K.K. Makesh, K. Ganesh Kumara: Physica B: Condensed Matter, Vol. 324, 2002, No. (1-4), p. 419-428, DOI: /10.1016/S0921-4526(02)01462-X
[10] R. Stalmans, J. Van Humbeeck, L. Delay: Scripta metallurgica et materialia, Vol. 31, 1994, No. (11), p. 1573-1576, DOI: 10.1016/0956-716X(94)90076-0
[11] G. Costanza, M.E. Tata: Procedia Structural Integrity, Vol. 2, 2016, p. 1451-1456, DOI: 10.1016/j.prostr.2016.06.184
[12] G. Costanza, M.E. Tata: Journal of intelligent materials and structures, Vol. 29, 2018, p. 1793-1798, DOI: 10.1177/1045389X17754262
[13] G. Costanza, G. Leoncini, F. Quadrini, M.E. Tata: Advances in materials science and engineering, 2017, art. N. 8467971, DOI: 10.1155/2017/8467971
[14] A. Boschetto, L. Bottini, G. Costanza, M.E. Tata: Actuators, Vol. 8, 2019, No. 2, article number 38, DOI: 10.3390/act8020038
[15] G. Bovesecchi, S. Coarasaniti, G. Costanza, M.E. Tata: Aerospace, Vol. 6, 2019, No. 7, article number 78, DOI: 10.3390/aerospace6070078
[16] B. Carpenter, J. Lyons: EO-1 technology validation report: lightweight flexible solar array experiment. Technical report NASA Godard Space Flight Center, Greenbelt, 2001
[17] J. N. Kudva: Journal of Intelligent Materials Systems and Structures, Vol. 15, 2004, p. 261-267, DOI: 10.1177/1045389X04042796
[18] D. Pitt, J. Dunne, E. White, E. Garcia: SAMPSON smart inlet SMA powered adaptive lip design and static test, Proceedings of 42th AIAA Structures, structural dynamics and material conference, Seattle, WA USA, 2001, 1-11.
[19] D. Hartl, B. Volk, D. C. Lagoudas, F.T. Calkins, J. Mabe: Shape memory alloy actuation for a variable area fan nozzle, Proceedings of SPIE, Smart Structures and Materials, Newport Beach, CA USA, 2001, 371-382.
[20] V. Brailovski, P. Terriault, T. Georges, D. Coutu: Physics Procedia, Vol. 10, 2010, p. 197-203, DOI: 10.1016/j.phpro.2010.11.098
[21] S. Saadat, J. Salichs, M. Noorl, Z. Hou, H. Davoodi, I. Baron: Smart Materials and Structures, Vol. 11, 2002, p. 218-229, DOI: 10.1088/0964-1726/11/2/305
[22] S.H. Youn, Y.S. Jang, J.H. Han: Journal of Intelligent Materials Systems and Structures, Vol. 21, 2010, No. 4, p. 407-421, DOI: 10.1177/1045389X09355665
[23] G. Costanza, S. Paoloni, M.E. Tata: Key Engineering Materials, Vol. 605, 2014, p. 23-26, DOI:10.4028/www.scientific.net/KEM.605.23
[24] R. Magerle: Fire & Smoke, 5, 2000, p. 28-33.